

1 **A comprehensive porewater isotope model for simulating benthic  
2 nitrogen cycling: Description, application to lake sediments, and  
3 uncertainty analysis**

4 Alessandra Mazzoli<sup>1</sup>, Peter Reichert<sup>2\*</sup>, Claudia Frey<sup>1</sup>, Cameron M. Callbeck<sup>1</sup>, Tim J. Paulus<sup>1</sup>, Jakob  
5 Zopfi<sup>1</sup>, Moritz F. Lehmann<sup>1</sup>

6 <sup>1</sup>Department of Environmental Sciences, University of Basel, Basel, 4056, Switzerland

7 <sup>2</sup>Eawag, Swiss Federal Institute of Aquatic Science and Technology, Dübendorf, 8600, Switzerland

8 \*Current status: retired from Eawag; email [peter.reichert@emeriti.eawag.ch](mailto:peter.reichert@emeriti.eawag.ch), see <https://peterreichert.github.io> for updated  
9 information

10 *Correspondence to:* Alessandra Mazzoli (alessandra.mazzoli@unibas.ch)

## 11 Abstract

12 The combination of various nitrogen (N) transformation pathways (mineralization, nitrification, denitrification, DNRA,  
13 anammox) modulates the fixed-N availability in aquatic systems, with important environmental consequences. Several  
14 models have been developed to investigate specific processes and estimate their rates, especially in benthic habitats, known  
15 hotspots for N-transformation reactions. Constraints on the N cycle are often based on the isotopic composition of N species,  
16 which integrates signals from various reactions. However, a comprehensive benthic N-isotope model, encompassing all  
17 canonical pathways in a stepwise manner, and including nitrous oxide, was still lacking. Here, we introduce a new diagenetic  
18 N-isotope model to analyse benthic N processes and their N-isotopic signatures, validated using field data from the  
19 porewaters of the oligotrophic Lake Lucerne (Switzerland). As parameters in such a complex model cannot all uniquely be  
20 identified from sparse data alone, we employed Bayesian inference to integrate prior parameter knowledge with data-derived  
21 information. For parameters where marginal posterior distributions considerably deviated from prior expectations, we  
22 performed sensitivity analyses to assess the robustness of these findings. Alongside developing the model, we established a  
23 methodology for its effective application in scientific analysis. For Lake Lucerne, the model accurately replicated observed  
24 porewater N-isotope and concentration patterns. We identified aerobic mineralization, denitrification, and nitrification as  
25 dominant processes, whereas anammox and DNRA played a less important role in surface sediments. Among the estimated  
26 N isotope effects, the value for nitrate reduction during denitrification was unexpectedly low ( $2.8 \pm 1.1\%$ ). We identified the  
27 spatial overlap of multiple reactions to be influential for this result.

28 **1 Introduction**

29 Nitrogen (N) is an essential element for all living organisms (Xu et al., 2022) and often limits primary production in aquatic  
30 systems (Kessler et al., 2014). In order to meet the global demand for fixed N (nitrate,  $\text{NO}_3^-$ , and ammonium,  $\text{NH}_4^+$ ),  
31 industrial fixation of atmospheric dinitrogen ( $\text{N}_2$ ) through the Haber-Bosch process now exceeds biological  $\text{N}_2$  fixation, with  
32 unforeseeable consequences regarding the ability of the environment to remove the excess fixed N, leaving the global N  
33 cycle imbalanced (Kessler et al., 2014). High fixed-N in aquatic systems has detrimental environmental consequences (Denk  
34 et al., 2017; Yuan et al., 2023), including eutrophication, ecosystem deterioration, and greenhouse gas emissions (e.g.,  
35 nitrous oxide,  $\text{N}_2\text{O}$ ). Thus, understanding the fate of fixed N in aquatic ecosystems and quantifying N fluxes are crucial for  
36 global budget estimates (Pätsch and Kühn, 2008).

37 In aquatic systems, benthic habitats are important hotspots in the transformation of large amounts of fixed N (Dale et al.,  
38 2019; Pätsch and Kühn, 2008; Xu et al., 2022), owing to sharp oxyclines and the co-occurrence of aerobic and anaerobic  
39 processes. The active N cycle in these sediments is driven by the flux of organic matter (OM) from the photic zone along  
40 with elevated concentrations of other electron donors (Ibánhez and Rocha, 2017; Wankel et al., 2015). Aerobic reactions,  
41 such as nitrification (stepwise  $\text{NH}_4^+$  oxidation to  $\text{NO}_3^-$  via nitrite,  $\text{NO}_2^-$ , with  $\text{N}_2\text{O}$  as by-product), are usually restricted to the  
42 top few millimetres in OM-rich sediments (e.g., in small lakes) or extend several centimetres deep in OM-poor sediments  
43 (e.g., in large oligotrophic lakes and the ocean) (Pätsch and Kühn, 2008; Wankel et al., 2015). The fate of  $\text{NO}_3^-$ , produced via  
44 nitrification either locally in the sediments or in the water column, determines a system's capacity to function as an efficient  
45 N sink (Wankel et al., 2015). Denitrification, the stepwise reduction of  $\text{NO}_3^-$  to  $\text{N}_2$  (via  $\text{NO}_2^-$  and  $\text{N}_2\text{O}$ ), has been identified as  
46 a key pathway for anaerobic N removal. Additionally, anammox, the anaerobic oxidation of  $\text{NH}_4^+$  to  $\text{N}_2$  using  $\text{NO}_2^-$ , can  
47 contribute to N loss (Ibánhez and Rocha, 2017; Kampschreur et al., 2012; Wankel et al., 2015), especially in oligotrophic  
48 lake sediments (Crowe et al., 2017). In anammox, partial oxidation of  $\text{NO}_2^-$  generates  $\text{NO}_3^-$  as a by-product to provide  
49 reducing equivalents for the fixation of inorganic carbon (C) (Brunner et al., 2013; Strous et al., 1999). Counteracting N  
50 removal by anammox and denitrification, the dissimilatory  $\text{NO}_3^-$  reduction to  $\text{NH}_4^+$  (DNRA) contributes to N retention  
51 (Denk et al., 2017; Ibánhez and Rocha, 2017; Rooth and Meile, 2016). The relative balance between these N-transforming  
52 reactions is strongly influenced by environmental conditions, particularly the ratio of organic C to  $\text{NO}_3^-$  and oxygen ( $\text{O}_2$ )  
53 availability. For instance, DNRA may be predominant under high C: $\text{NO}_3^-$  ratios (Ibánhez and Rocha, 2017; Kraft et al.,  
54 2011; Wang et al., 2020). Oxygen is a central regulator in this context: it controls the coupling of nitrification with  
55 denitrification, anammox and DNRA, and modulates  $\text{N}_2\text{O}$  production and consumption, with peak  $\text{N}_2\text{O}$  yields typically  
56 occurring at the oxic-anoxic interface (Ni et al., 2011). The spatial overlap of aerobic and anaerobic N cycling processes at  
57 this transition zone in sediments often results in very low concentrations of metabolic intermediates (e.g.,  $\text{N}_2\text{O}$ ) in porewater,  
58 complicating their measurements in natural benthic environments. This is particularly true for the analysis of natural-  
59 abundance DIN isotopologues, which provide critical insights into N-cycling reactions and pathways. However, measuring  
60 these isotopologues, especially low-concentration intermediates in porewater, is technically challenging, if not impossible at

61 **present**, To overcome these limitations, isotope modelling has become an essential tool for quantifying rapid N turnover at  
62 the oxic-anoxic interface, and for evaluating environmental controls on N dynamics and isotope signatures across diverse  
63 settings (Denk et al., 2017; Wankel et al., 2015).

**Deleted:** all

64 Natural abundance stable isotope measurements provide insights into the N cycle, and the fluxes within its pathways, as  
65 microbial processes impart unique isotopic imprints on the involved N pools (Lehmann et al., 2003; Rooze and Meile, 2016;  
66 Wankel et al., 2015). In most microbial processes, the isotopically lighter molecules are preferentially consumed, yielding  
67  $^{15}\text{N}$ -depleted products and  $^{15}\text{N}$ -enriched substrates (normal N-isotopic fractionation) (Kessler et al., 2014), with few  
68 exceptions, such as  $\text{NO}_2^-$  oxidation, which occurs with an inverse N isotope fractionation (Casciotti, 2009; Martin et al.,  
69 2019). The isotopic composition of a given N pool is expressed in  $\delta$ -notation,  $\delta^{15}\text{N}$  (‰ vs. std) =  $[(R_{\text{sample}}/R_{\text{std}}) - 1] \times 1000$ ,  
70 where  $R$  is the isotope ratio  $^{15}\text{N}/^{14}\text{N}$ , and the internationally recognized standard is atmospheric  $\text{N}_2$  (Denk et al., 2017; Martin  
71 et al., 2019). The extent of the isotopic fractionation for a reaction is quantified using the isotope effect,  $\varepsilon$ , defined as  $\varepsilon$  (‰) =  
72  $[1 - ({}^Hk/{}^Lk)] \times 1000$ , where  ${}^Hk$  and  ${}^Lk$  are the specific reaction rates for the isotopically heavy and light molecules,  
73 respectively (Sigman and Fripiat, 2019). For instance,  $\delta^{15}\text{N-NO}_2^-$  analysis can help differentiate reductive and oxidative  
74 pathways of  $\text{NO}_2^-$  consumption, as they are characterised by a normal and an inverse kinetic isotope effect, respectively  
75 (Dale et al., 2019; Martin et al., 2019; Rooze and Meile, 2016). Despite considerable efforts to estimate isotope effects for  
76 most N-transformation processes (Denk et al., 2017), isotope effects estimated in batch cultures often differ from in situ  
77 measurements (Martin et al., 2019). To date, **only limited efforts have been made to develop** comprehensive benthic isotope  
78 **models** that integrate **multiple N-transformation processes in a stepwise manner, and assess** the expression of their isotope  
79 effects in the porewater of aquatic sediments, validated with observational data (Denk et al., 2017; **Rooze and Meile, 2016**).

80 Existing N-isotope models address specific aspects of the N cycle (Denk et al., 2017), such as denitrification (Kessler et al.,  
81 2014; Lehmann et al., 2003; Wankel et al., 2015),  $\text{NO}_2^-$  oxidation and reduction (Buchwald et al., 2018) or  $\text{N}_2\text{O}$  dynamics  
82 (Ni et al., 2011; Wunderlin et al., 2012). As denitrification is the primary pathway for fixed-N loss in many aquatic systems,  
83 models integrating dual  $\text{NO}_3^-$  isotopes (Lehmann et al., 2003; Wankel et al., 2015) have been used for example, to constrain  
84 its partitioning between water-column and benthic denitrification (Lehmann et al., 2005), as well as the contribution of  
85 regenerated  $\text{NO}_3^-$  supporting denitrification (Lehmann et al., 2004). Rooze and Meile (2016) combined isotope data with a  
86 reaction-transport model to investigate the influence of hydrodynamics on fixed-N removal, highlighting enhanced coupling  
87 of nitrification- $\text{N}_2$  production by benthic infauna. Buchwald et al. (2018) used dual  $\text{NO}_3^-$  and  $\text{NO}_2^-$  isotope analyses, and a  
88 reaction-diffusion model to demonstrate the tight coupling of  $\text{NO}_3^-$  reduction and  $\text{NO}_2^-$  oxidation near oxic-anoxic interfaces,  
89 emphasizing the central role of  $\text{NO}_2^-$  in N recycling. In contrast, most  $\text{N}_2\text{O}$  modelling efforts (primarily concentration-based  
90 models) to date have focused on engineered systems such as wastewater treatment, where they have been used to assess  $\text{N}_2\text{O}$   
91 production pathways under variable conditions, and to minimize its emissions (Ni et al., 2011; Wunderlin et al., 2012).  
92 Challenges in measuring  $\text{N}_2\text{O}$  isotopologues in natural settings, especially in sediment porewaters, have limited the broader  
93 application of  $\text{N}_2\text{O}$  isotopic approaches and led to the exclusion of  $\text{N}_2\text{O}$  from benthic N-isotope modelling efforts so far.  
94 Nonetheless, given the key role of  $\text{N}_2\text{O}$  in the N cycle, and its sensitivity to redox conditions, there is a growing need for

**Deleted:** a

**Deleted:** s

**Deleted:** , is still lacking

99 modelling frameworks that integrate multi-species N-isotope dynamics, even in the absence of direct measurements of N-  
100 cycle intermediate like  $\text{NO}_2^-$  and  $\text{N}_2\text{O}$  to more accurately capture the interconnected nature of N transformations in natural  
101 systems.

102 With this study, we introduce a comprehensive 1-D diffusion-reaction model, encompassing all canonical N-transformation  
103 processes and most DIN isotopologues, to assess the role of distinct environmental factors (e.g., ~~OM~~ reactivity, bioturbation)  
104 in shaping porewater N dynamics and the N isotopic signatures of the different N transformations (and combinations thereof)  
105 generate. Furthermore, by considering the stepwise nature of the N-cycling pathways, the model quantifies and isotopically  
106 characterizes key intermediates (i.e.,  $\text{N}_2\text{O}$ ,  $\text{NO}_2^-$ ), which serve as substrates for subsequent reactions (Martin et al., 2019).  
107 Moreover, the model acts as a valuable research tool for analysing process couplings (e.g., DNRA-anammox interactions)  
108 (Dale et al., 2019; Hines et al., 2012), which are crucial for accurately estimating N removal and recycling, and can influence  
109 the apparent isotope effects of  $\text{NO}_3^-$  and  $\text{NO}_2^-$ . Incorporating  $\text{N}_2\text{O}$  isotopologues as state variables enables the model to  
110 resolve the relative importance of  $\text{N}_2\text{O}$  producing mechanisms across small-scale benthic oxic-anoxic interfaces, and to  
111 quantify their contribution to sedimentary  $\text{N}_2\text{O}$  emissions.

112 The application of a comprehensive diagenetic N isotope model to measured porewater profiles of selected inorganic N  
113 compounds often results in parameter identifiability issues. Specifically, similar fits to the observed data might be achieved  
114 with comparable accuracy using different parameter sets, each yielding distinct transformation rates. To reduce the risk of  
115 drawing erroneous conclusions from such identifiability problems, we employed the following modelling strategies:

116 • *Use of prior knowledge*

117 Prior knowledge informed both the development of the model structure and the selection of parameter values. The  
118 model parameterization was adapted as deemed necessary to effectively integrate this prior knowledge. This  
119 approach aims to produce a plausible representation of the mechanisms governing the data.

120 • *Consideration of uncertainty*

121 Uncertainty in model parameters was explicitly accounted for using epistemic probability distributions. Bayesian  
122 inference (Bernardo and Smith, 1994; Gelman et al., 2013; Robert, 2007) was employed to combine prior  
123 knowledge with information obtained from observational data. The resulting posterior distribution of the parameters  
124 and calculated results provide a comprehensive uncertainty description, which is, however, still conditioned on prior  
125 information about the model structure and parameters.

126 • *Sensitivity analysis*

127 To test the robustness of key results against modelling assumptions, we assessed their sensitivity to the choice of  
128 prior probability distribution of the model parameters and to the inclusion of specific active processes within the  
129 model.

130 Since the numerical implementation of Bayesian inference requires the computationally intensive Markov Chain Monte  
131 Carlo (MCMC) sampling technique (Andrieu et al., 2003), an efficient model implementation is required. To meet this need,  
132 we implemented the model in Julia (Bezanson et al., 2017) (<https://julialang.org>), a high-performance programming

**Deleted:** sediment

language. This choice also enables the use of automatic differentiation, which supports advanced MCMC techniques like Hamiltonian Monte Carlo (HMC) (Betancourt, 2017; Neal, 2011). The model was tested using field measurements from oligotrophic Lake Lucerne. It is important to emphasize that this isotope model is designed as a research tool, rather than a predictive instrument. Its primary purpose is to test hypotheses and assumptions related to the biogeochemical controls on N isotope signatures in natural environments, and to assess the identifiability of process rates and N isotope effects from observational data.

## 2 Model description

### 2.1 Model formulation

A one-dimensional diffusion-reaction model was developed to simulate the concentrations of inorganic N compounds ( $\text{NO}_3^-$ ,  $\text{NO}_2^-$ ,  $\text{NH}_4^+$ ,  $\text{N}_2$ ,  $\text{N}_2\text{O}$ ), distinguishing between  $^{14}\text{N}$  and  $^{15}\text{N}$  isotopes ( $^{14}\text{NO}_3^-$ ,  $^{15}\text{NO}_3^-$ ,  $^{14}\text{NO}_2^-$ ,  $^{15}\text{NO}_2^-$ ,  $^{14}\text{NH}_4^+$ ,  $^{15}\text{NH}_4^+$ ,  $^{14}\text{N}_2$ ,  $^{14}\text{N}^{15}\text{N}$ ,  $^{15}\text{N}_2$ ,  $^{14}\text{N}_2\text{O}$ ,  $^{14}\text{N}^{15}\text{NO}$ ,  $^{15}\text{N}_2\text{O}$ ), as well as for  $\text{O}_2$  and sulfate ( $\text{SO}_4^{2-}$ ) concentrations. Their production and consumption rates are described by incorporating key processes of the canonical N cycle: aerobic mineralization, denitrification, nitrification, anammox, DNRA, mineralization by  $\text{SO}_4^{2-}$  reduction, and anaerobic mineralization (other than  $\text{SO}_4^{2-}$ -driven) (Fig. 1). All reactions (Table 1) are described using the general formula:

$$\text{rate} = k_{max} \cdot \text{limitation} \cdot \text{inhibition} \quad (1)$$

where  $k_{max}$  represents the maximum conversion rate under ideal conditions (in  $\mu\text{M d}^{-1}$ ). The terms for limitation by substrate X and inhibition by substance Y for the process i are defined following Michaelis-Menten kinetics (Martin et al., 2019):

$$\text{limitation} = \frac{[X]}{K_{X,i} + [X]} \quad (2)$$

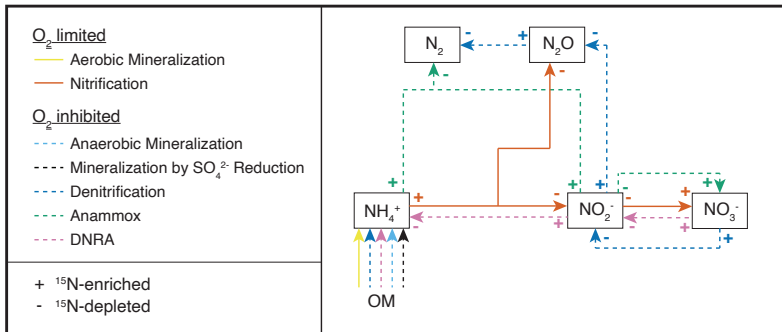
$$\text{inhibition} = \frac{K_{Y,i}}{K_{Y,i} + [Y]} \quad (3)$$

where  $[X]$  and  $[Y]$  are the concentrations (in  $\mu\text{M}$ ) of substances X and inhibitor Y, respectively, while  $K_{X,i}$  and  $K_{Y,i}$  are their respective half-saturation and inhibition constants (in  $\mu\text{M}$ ) for process i, respectively. While the model supports exponential equations for limitation and inhibition terms, Michaelis-Menten kinetics were chosen for this study, as they are more commonly employed in N models (Rooze and Meile, 2016). The specific reaction rate equations are implemented taking into account the concentrations of  $^{14}\text{N}$ ,  $^{15}\text{N}$ ,  $^{14}\text{N}^{14}\text{N}$ ,  $^{14}\text{N}^{15}\text{N}$ , and  $^{15}\text{N}^{15}\text{N}$  species separately for the limitation term. For  $^{15}\text{N}$ -containing species, specific reaction rates are reduced by  $(1-\varepsilon/1000)$  relative to  $^{14}\text{N}$ -containing species, reflecting the isotope effect associated with a given reaction (detailed descriptions of the model processes are provided in Appendix A: *Model processes and stoichiometry*).

Molecular diffusion is modelled taking into account the reduced solute movement due to tortuosity (Burdige, 2007). Additionally, bioturbation is included as a transport term enhancing diffusion, with its influence exponentially decreasing with depth. Boundary conditions are set based on observed concentrations of N compounds,  $\text{O}_2$ ,  $\text{SO}_4^{2-}$  at the upper boundary, and by zero fluxes at the lower boundary, except for  $\text{NH}_4^+$ . The  $\text{NH}_4^+$  flux (and its  $\delta^{15}\text{N}_{\text{NH}_4^+}$ ) was jointly estimated with the

**Deleted:** ,  
**Deleted:** t  
**Deleted:** of which

167 model parameters, as the field data display a clear  $\text{NH}_4^+$  concentration gradient at 5 cm. Total N,  $^{14}\text{N}$  and  $^{15}\text{N}$  concentrations,  
 168 along with their fluxes, are used for model parameterization (see Appendix B: *Reaction-diffusion model* for details).  
 169 The model is formulated as a dynamic model, but simulated to steady-state for comparison with observational data.  
 170 Concentrations of  $^{14}\text{N}$ - and  $^{15}\text{N}$ -containing compounds are converted to total concentrations and  $\delta^{15}\text{N}$ .



171  
 172 Figure 1: Simplified scheme of the N-transformation reactions considered for the diagenetic isotope model described in this paper.  
 173 Continuous lines identify aerobic processes, while dashed lines indicate anaerobic processes. The state variables explicitly modelled  
 174 as substrates for the considered reactions are highlighted with outlined boxes;  $\text{O}_2$  is modelled as a state variable and as a regulator  
 175 of aerobic and anaerobic processes; organic matter (OM) is not a state variable *per se* within the framework of this model, but acts  
 176 as a source of N for the remaining processes. The isotopic fractionation of each process is shown using + and - signs to represent  
 177 the  $^{15}\text{N}$ -enriching and  $^{15}\text{N}$ -depleting effects of the respective reactions.

## 178 2.2 Description of modelled transformation processes

179 This section outlines the modelled processes for  $^{14}\text{N}$  and  $^{14}\text{N}^{15}\text{N}$  compounds (Table 1). A comprehensive overview of the  
 180 transformation processes for all isotopologues, and stoichiometric relations is provided in Appendix A: *Model processes and*  
 181 *stoichiometry*.

182 Mineralization of OM, the sole external N source, is differentiated in the model according to the specific electron acceptor  
 183 involved: aerobic mineralization ( $\text{O}_2$ ), denitrification and DNRA ( $\text{NO}_3^-$ ),  $\text{SO}_4^{2-}$  reduction, and anaerobic mineralization. The  
 184 latter encompasses all remaining redox species (i.e., other than  $\text{O}_2$ ,  $\text{NO}_3^-$ , and  $\text{SO}_4^{2-}$ ) below the nitracline (e.g., manganese,  
 185 iron oxides, carbon dioxide).

186 Denitrification is modelled as a three-step process: (1)  $\text{NO}_3^-$  to  $\text{NO}_2^-$ ; (2)  $\text{NO}_2^-$  to  $\text{N}_2\text{O}$ ; and (3)  $\text{N}_2\text{O}$  to  $\text{N}_2$ . The first step,  
 187 typically regarded as the rate-limiting step (Kampschreur et al., 2012), is the primary control on the overall expression of the  
 188 N isotope effect (Kessler et al., 2014; Rooze and Meile, 2016). To prevent unrealistic rates, subsequent steps are constrained  
 189 by setting  $k_{\text{Den}2} = f_{\text{Den}2} \times k_{\text{Den}1}$  and  $k_{\text{Den}3} = f_{\text{Den}3} \times k_{\text{Den}1}$ , and specifying priors for  $f_{\text{Den}2}$  and  $f_{\text{Den}3}$ . The re-parameterization of the  
 190 second and third steps using the  $f_{\text{Den}2\text{Den}1}$  and  $f_{\text{Den}3\text{Den}1}$  factors corresponds to exactly the same model without any  
 191 approximation or simplification. It serves solely to facilitate the specification of priors, as more knowledge is typically

192 available about ratios of maximum rates (i.e.,  $f_{Den2Den1} = k_{Den2}/k_{Den1}$ ) than about the absolute maximum rates themselves. The  
193  $\text{NO}_3^-$  N isotope effect during benthic denitrification is known to be suppressed in the overlying water due to diffusion  
194 limitation (Dale et al., 2022; Kessler et al., 2014; Lehmann et al., 2003), though its expression at the porewater level remains  
195 less well constrained (Winkel et al., 2015). Transiently accumulating intermediates, such as  $\text{N}_2\text{O}$ , that can escape to the  
196 overlying water and alter benthic N fluxes (Rooze and Meile, 2016), are also considered. Lastly, to ensure mass balance, the  
197 model accounts for clumped (doubly substituted; e.g.,  $^{15}\text{N}^{15}\text{NO}$  and  $^{15}\text{N}^{15}\text{N}$ ) isotopocules, but does not distinguish between  
198 isotopomers (i.e.,  $^{14}\text{N}^{15}\text{NO}$  and  $^{15}\text{N}^{14}\text{NO}$ ) due to lack of  $\text{N}_2\text{O}$  isotope data needed for model validation. For the purpose of  
199 comparison with previous N models, a simplified one-step denitrification pathway ( $\text{NO}_3^-$  to  $\text{N}_2$  with no release of  $\text{NO}_2^-$  or  
200  $\text{N}_2\text{O}$  into the environment) approach is also implemented in the model code.

201 Nitrification is modelled as a two-step process: (1a)  $\text{NH}_4^+$  to  $\text{NO}_2^-$ ; (1b)  $\text{NH}_4^+$  to  $\text{N}_2\text{O}$ ; (2)  $\text{NO}_2^-$  to  $\text{NO}_3^-$ . As for  
202 denitrification, the second step of nitrification is constrained to prevent unrealistic rates:  $k_{Nit2} = f_{Nit2} \times k_{Nit1}$ , with specifying a  
203 prior for  $f_{Nit2}$ .  $\text{N}_2\text{O}$  production yield during the first step is  $\text{O}_2$ -dependent, and is modelled accordingly:

$$204 \quad f_{N2O\_Nit1} = \frac{b \ a}{[\text{O}_2] + a} \quad (4)$$

205 where  $b$  and  $a$  are empirical parameters derived from (Ji et al., 2018).  $\text{N}_2\text{O}$  production also occurs via nitrification-  
206 denitrification, implicitly modelled by allowing reaction coupling via the intermediate  $\text{NO}_2^-$ . The expression of isotope  
207 effects depends on substrate availability and reaction completion. For instance, incomplete nitrification has been shown to  
208 result in isotopically heavy  $\text{NH}_4^+$  efflux from the sediments (Dale et al., 2022; Lehmann et al., 2004; Rooze and Meile,  
209 2016). However, similar phenomena for  $\text{N}_2\text{O}$  and  $\text{NO}_2^-$  remain poorly understood.

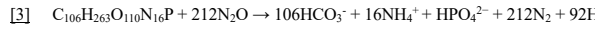
210 The limited understanding of porewater N isotope dynamics, especially for processes other than denitrification, hinges on the  
211 scarcity of isotope data for crucial N species like  $\text{NH}_4^+$  and  $\text{NO}_2^-$  in natural settings (Martin et al., 2019; Winkel et al., 2015).  
212 In the present model, we investigated the importance of these solutes, and how N-turnover processes like DNRA and  
213 anammox shape the distribution of their N isotopes. DNRA is modelled as a two-step process: (1)  $\text{NO}_3^-$  to  $\text{NO}_2^-$ ; and (2)  
214  $\text{NO}_2^-$  to  $\text{NH}_4^+$ . This approach separates the impact of  $\text{NO}_2^-$  reduction on  $\text{NH}_4^+$ , and allows comparison of  $\text{NO}_2^-$  isotopic  
215 signatures induced by denitrification, DNRA, and anammox. Anammox is modelled to include [both the comproportionation](#)  
216 [of  \$\text{NH}\_4^+\$  and  \$\text{NO}\_2^-\$  to  \$\text{N}\_2\$  \(main reaction, “m”\), and the](#)  $\text{NO}_3^-$  production via  $\text{NO}_2^-$  oxidation [\(side reaction, “s”\)](#) (0.3 mol  $\text{NO}_3^-$   
217 produced per 1 mol  $\text{NH}_4^+$  and 1.3 mol  $\text{NO}_2^-$ ) ([Tables 1 and A1](#)) (Martin et al., 2019), which imparts a strong inverse isotope  
218 fractionation (Brunner et al., 2013; Magyar et al., 2021).

219 The relative importance of reductive  $\text{NO}_3^-$  pathways is constrained by altering maximum conversion rates,  $k$ , as:  $k_{DNRA1} =$   
220  $f_{DNRA1,Den1} \times k_{Den1}$ ;  $k_{DNRA2} = f_{DNRA2,Den2} \times k_{Den2}$ ;  $k_{Anam} = f_{Anam,Den2} \times k_{Den2}$ , where prior information on  $f$  factors was obtained from  
221 experimental rate measurements (see below). Altogether these reactions provide a comprehensive overview of N isotope  
222 dynamics in porewater and enable the assessment of influential environmental conditions in shaping them.

223 **Table 1: Chemical equations and reaction rate formulations for  $^{14}\text{N}$  and  $^{14}\text{N}^{14}\text{N}$  compounds across all modelled processes.** The  
224 rates for  $^{15}\text{N}$ ,  $^{15}\text{N}^{14}\text{N}$ , and  $^{15}\text{N}^{15}\text{N}$  are formulated analogously by replacing the concentration of the isotopologue of interest as  
225 needed. The turnover rates for  $^{15}\text{N}$ -containing species are scaled by a factor of (1- $\delta/1000$ ), as outlined in the text. The complete set  
226 of equations including all isotopic compositions, and the process stoichiometry is provided in Appendix A: *Model processes and*

227 **stoichiometry.** Anaerobic mineralization encompasses OM degradation coupled to iron and manganese reduction, as well as  
 228 through methanogenesis.

Reaction	Equation	Reaction rate
<u>Aerobic mineralization</u>	$C_{106}H_{263}O_{110}N_{16}P + 106O_2 \rightarrow 106HCO_3^- + 16NH_4^+ + HPO_4^{2-} + 92H^+$	
		$r_{MinOx} = k_{MinOx} \frac{[O_2]}{K_{O2,MinOx} + [O_2]}$
<u>Anaerobic Mineralization</u>	$C_{106}H_{263}O_{110}N_{16}P + 212MnO_2 + 120H_2O \rightarrow 106HCO_3^- + 16NH_4^+ + HPO_4^{2-} + 212Mn^{2+} + 332OH^-$	
	$C_{106}H_{263}O_{110}N_{16}P + 424FeOOH + 120H_2O \rightarrow 106HCO_3^- + 16NH_4^+ + HPO_4^{2-} + 424Fe^{2+} + 332OH^-$	
	$C_{106}H_{263}O_{110}N_{16}P \rightarrow 53CH_4^+ + 53HCO_3^- + 16NH_4^+ + HPO_4^{2-} + 53H_2O + 14H^+$	
		$r_{MinAnae} = k_{MinAnae} \frac{K_{NO_3,MinAnae}}{K_{NO_3,MinAnae} + [^{14}NO_3^-] + [^{15}NO_3^-]} \frac{K_{O2,MinAnae}}{K_{O2,MinAnae} + [O_2]}$
<u>Sulfate Reduction coupled to Mineralization</u>	$C_{106}H_{263}O_{110}N_{16}P + 53SO_4^{2-} + 15H^+ \rightarrow 106HCO_3^- + 16NH_4^+ + HPO_4^{2-} + 53H_2S$	
		$r_{MinSulfRed} = k_{MinSulfRed} \frac{K_{NO_3,MinSulfRed}}{K_{NO_3,MinSulfRed} + [^{14}NO_3^-] + [^{15}NO_3^-]} \frac{K_{O2,MinSulfRed}}{K_{O2,MinSulfRed} + [O_2]} \frac{[SO_4^{2-}]}{K_{SO_4,MinSulfRed} + [SO_4^{2-}]}$
<u>Nitrification</u>	<u>[1a]</u> $NH_4^+ + 1.5O_2 \rightarrow NO_2^- + 2H^+ + H_2O$	
		$r_{Nit1a} = k_{Nit1} (1 - f_{N2O,Nit1}) \frac{[^{14}NH_4^+]}{K_{NH_4,Nit1} + [^{14}NH_4^+] + [^{15}NH_4^+]} \frac{[O_2]}{K_{O2,Nit1} + [O_2]}$
	<u>[1b]</u> $NH_4^+ + O_2 \rightarrow 0.5N_2O + H^+ + 1.5H_2O$	
		$r_{Nit1b} = k_{Nit1} f_{N2O,Nit1} \frac{[^{14}NH_4^+] [^{14}NH_4^+]}{(K_{NH_4,Nit1} + [^{14}NH_4^+] + [^{15}NH_4^+])^2} \frac{[O_2]}{K_{O2,Nit1} + [O_2]}$
	<u>[2]</u> $NO_2^- + 0.5O_2 \rightarrow NO_3^-$	
		$r_{Nit2} = k_{Nit2} \frac{[^{14}NO_2^-]}{K_{NO_2,Nit2} + [^{14}NO_2^-] + [^{15}NO_2^-]} \frac{[O_2]}{K_{O2,Nit2} + [O_2]}$
<u>Denitrification</u>	<u>[1]</u> $5C_{106}H_{263}O_{110}N_{16}P + 424NO_3^- \rightarrow 212HCO_3^- + 32NH_4^+ + 2HPO_4^{2-} + 424NO_2^- + 184H^+ + 3C_{106}H_{263}O_{110}N_{16}P$	
		$r_{Den1} = k_{Den1} \frac{[^{14}NO_3^-]}{K_{NO_3,Den1} + [^{14}NO_3^-] + [^{15}NO_3^-]} \frac{K_{O2,Den1}}{K_{O2,Den1} + [O_2]}$
	<u>[2]</u> $3C_{106}H_{263}O_{110}N_{16}P + 424NO_2^- + 240H^+ \rightarrow 212HCO_3^- + 32NH_4^+ + 2HPO_4^{2-} + 212N_2O + 212H_2O + C_{106}H_{263}O_{110}N_{16}P$	
		$r_{Den2} = k_{Den2} \frac{[^{14}NO_2^-]^2}{(K_{NO_2,Den2} + [^{14}NO_2^-] + [^{15}NO_2^-])^2} \frac{K_{O2,Den2}}{K_{O2,Den2} + [O_2]}$

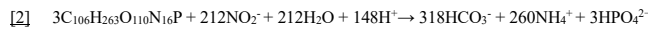


$$r_{Den3} = k_{Den3} \frac{[\text{^{14}N}_2\text{O}]}{K_{N2O,Den3} + [\text{^{14}N}_2\text{O}] + [\text{^{14}N}_2\text{O}] + [\text{^{15}N}_2\text{O}]} \frac{K_{O2,Den3}}{K_{O2,Den3} + [\text{O}_2]}$$

DNRA

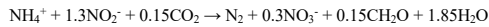


$$r_{DNRA1} = k_{DNRA1} \frac{[\text{^{14}NO}_3^-]}{K_{NO3,DNRA1} + [\text{^{14}NO}_3^-] + [\text{^{15}NO}_3^-]} \frac{K_{O2,DNRA1}}{K_{O2,DNRA1} + [\text{O}_2]}$$



$$r_{DNRA2} = k_{DNRA2} \frac{[\text{^{14}NO}_2^-]}{K_{NO2,DNRA2} + [\text{^{14}NO}_2^-] + [\text{^{15}NO}_2^-]} \frac{K_{O2,DNRA2}}{K_{O2,DNRA2} + [\text{O}_2]}$$

Anammox



$$r_{Anam} = k_{Anam} \frac{[\text{^{14}NH}_4^+]}{K_{NH4,Anam} + [\text{^{14}NH}_4^+] + [\text{^{15}NH}_4^+]} \frac{[\text{^{14}NO}_2^-]}{K_{NO2,Anam} + [\text{^{14}NO}_2^-] + [\text{^{15}NO}_2^-]} \frac{K_{O2,Anam}}{K_{O2,Anam} + [\text{O}_2]}$$

229 2.3 Model assumptions

230 The model builds on the following considerations and assumptions:

- 231 i. The inputs of sinking OM and associated advective transport relative to the sediment surface are not explicitly  
232 modelled, as the dissolved O<sub>2</sub> and N-compound profiles tend to reach quasi-steady state on short timescales (days to  
233 weeks). This simplification may not be valid for continental shelf sediments, where advection dominates solute  
234 movement due to high sediment permeability (Rooze and Meile, 2016). Therefore, in our model, porewater profiles  
235 are shaped primarily by molecular diffusion and bioturbation (the latter approximated as enhanced diffusion), along  
236 with reaction processes.
- 237 ii. Hinging on assumption i., the rates of OM-degrading processes are assumed to be limited by the availability of  
238 oxidants and not of OM, as in Kessler et al. (2014), an assumption that holds for sediments with sufficient readily  
239 degradable OM, but may break down at great depths. As OM is neither a state variable nor a limiting substrate, its  
240 production and consumption rates are not tracked and are considered uninfluential within the current model.
- 241 iii. Microorganisms involved in N-transformation pathways are not explicitly modelled, meaning that maximum  
242 conversion rates, *k*, represent a combination of bacterial maximum specific growth rates and abundance. These  
243 parameters likely vary significantly across systems, due to differences in OM loading. Variabilities in cell-specific  
244 rates, and consequently in isotope effects, over depth and substrate availability were not considered.
- 245 iv. N assimilation is not included, which is plausible if the turnover rates of the modelled processes are considerably  
246 higher than the N assimilation rates.
- 247 v. Maximum specific conversion rates for all reactions are constant with depth, implying uniform bacterial abundance  
248 and activity across the sediment layer affected by any given process.

**Deleted:** .

250 vi. Limitation and inhibition kinetics are modelled using Michaelis-Menten functions, as they are commonly employed  
251 in N-cycle models (Rooze and Meile, 2016); exponential equations are provided within the code as an alternative  
252 approach, depending on user preference.

253 vii. OM composition is approximated by the Redfield ratio (C:N:P = 106:16:1), used to estimate the fraction of  $\text{NH}_4^+$   
254 released during OM mineralization.<sup>1,2</sup>

255 viii. Anaerobic mineralization includes all processes involving redox species below the nitracline (e.g., manganese, iron,  
256 and carbon dioxide) with the exception of  $\text{SO}_4^{2-}$  reduction, with no distinction in reaction rate for different oxidants.  
257 Reduction of  $\text{SO}_4^{2-}$  is modelled separately, as it can occur at faster rates than oxidation by iron(III),  $\text{Fe}^{3+}$ , and  
258 manganese,  $\text{Mn}^{4+}$ , in some lacustrine systems (Steinsberger et al., 2020), and is the dominant anaerobic  
259 mineralization process in marine settings.

**Deleted:** <sup>3</sup>

260 ix. Re-oxidation of reduced species other than  $\text{NH}_4^+$  and  $\text{NO}_2^-$  (e.g.,  $\text{Fe}^{2+}$ ,  $\text{Mn}^{2+}$ ,  $\text{H}_2\text{S}$ ,  $\text{CH}_4$ ) is neglected in the  $\text{O}_2$   
261 budget for the modelled interval; this is appropriate where their upward fluxes are minor, but may underestimate  $\text{O}_2$   
262 demand in settings with substantial reduced-species fluxes. Future users are encouraged to adapt the model to their  
263 research questions and dataset, including adding processes and state variables, provided that they can be  
264 constrained.

**Deleted:** <#>N isotope effects for all processes are kept constant  
across depth and substrate availability.<sup>4</sup>

265 x. OM mineralization occurs with no N isotopic fractionation; that is, the released  $\text{NH}_4^+$  has the same N isotopic  
266 composition of OM, which is a model parameter considered for estimation.

267 xi. Diffusivities of isotopologues are considered identical, as their differences have been reported to be minimal  
268 (Lehmann et al., 2007; Winkel et al., 2015).

269 xii. Bioturbation enhances diffusion equally for all modelled species. As no solid was included as a state variable of the  
270 model, the impact of bioturbation on solid phase mixing was neglected.

271 xiii. The yield of  $\text{NO}_3^-$  during anammox is fixed at 0.3 mol  $\text{NO}_3^-$  per 1 mol  $\text{NH}_4^+$ , although reported values range from  
272 0.26 to 0.32 (Brunner et al., 2013).

273 xiv. The  $\text{NO}_3^-$  and  $\text{NO}_2^-$  equilibrium during anammox has been previously reported to occur under environmental stress  
274 conditions with a strong isotopic fractionation (up to  $\sim$ 60.5%) (Brunner et al., 2013). Since it leads to the production  
275 of  $^{15}\text{N}$ -enriched  $\text{NO}_3^-$ , similarly to the kinetic isotopic fractionation during  $\text{NO}_2^-$  oxidation to  $\text{NO}_3^-$ , variable values  
276 of  $\varepsilon_{\text{Anam},\text{side}}$  ( $-15\%$  to  $-45\%$ ) can encompass both kinetic and equilibrium fractionation.

277 xv.  $\text{NH}_4^+$  adsorption and desorption rates are assumed to be comparable, and to occur with negligible isotopic  
278 fractionation, resulting in no net effect on the  $\text{NH}_4^+$  pool concentration or isotopic composition.

279 The model incorporates deliberate simplifications to reduce complexity, while remaining adaptable to new data or insights;  
280 however, it is acknowledged that these assumptions may significantly influence model outcomes and should be carefully  
281 considered when interpreting results.

285 **2.4 Prior knowledge about model parameters**

286 Model parameter values were derived from an extensive literature review, and formulated as prior distributions, as detailed  
 287 and referenced in Appendix C: *Prior values for inference*. Positive parameters were parameterized as Lognormal priors,  
 288 while priors of positive or negative parameters were parameterized as Normal distributions. Mean values were derived from  
 289 the provided references, standard deviations were assigned either as absolute values or as percentages of the mean,  
 290 depending on the class of variables. For parameters that are lake-specific (see model assumption iii.) and expected to be well  
 291 identifiable from data, such as the maximum conversion rates of various processes (i.e., aerobic mineralization, the first step  
 292 of nitrification, the first step of denitrification, mineralization by  $\text{SO}_4^{2-}$  reduction, anaerobic mineralization) and the  $\text{NH}_4^+$   
 293 flux from deeper sediment layers, only limited prior knowledge is available, making the use of uniform priors preferable. As  
 294 their interpretability can be questionable, uniform priors were applied only to parameters expected to be well-identifiable,  
 295 ensuring that prior variations within the marginal posterior range would remain small, even with alternative broad priors.  
 296 This approach avoids specifying typical expected values, while maintaining robust identifiability. The maximum conversion  
 297 rates for anammox, DNRA, as well as the second step of nitrification and the second and third steps of denitrification  
 298 (Anam, DNRA1, DNRA2, Nit2, Den2 and Den3) were more challenging to identify from data, as the sensitivity of model  
 299 results to these parameters becomes very low when the concentration of the converted substance becomes small.  
 300 Additionally, prior specification for these rates was difficult, due to the expected variability among different lakes, similar to  
 301 other maximum conversion rate parameters. Therefore, their priors were formulated as ratios relative to the better-  
 302 constrained maximum conversion rate of the first nitrification (i.e.,  $k_{\text{Nit}}$ ) or denitrification step (i.e.,  $k_{\text{Den}}$ ). This approach  
 303 allowed for the characterization of the relative importance of each process without requiring absolute rate values. The joint  
 304 prior for all parameters was assumed to be an independent combination of their respective marginal prior distributions.

305 **2.5 Model-based analysis process**

306 To partially reduce structural uncertainty of the model and to account for parameter non-identifiability, Bayesian inference  
 307 was applied, considering all uncertain parameters listed in Appendix C: *Prior values for inference*. Some parameters were  
 308 excluded from this analysis, including molecular diffusion coefficients, compound concentrations at the sediment surface,  
 309 zero fluxes from deeper sediment layers (except for the  $\text{NH}_4^+$  flux, which was inferred jointly with other parameters) and  
 310 bioturbation. These values are considerably less uncertain than the other model parameters, except for bioturbation, which  
 311 was addressed separately through a scenario analysis, following Bayesian inference under the Base scenario.

312 The posterior distribution (probability density) of the model parameters,  $f_{\text{post}}$ , is expressed as

$$313 \quad f_{\text{post}}(\theta) = \frac{f_L(C|\theta) f_{\text{pri}}(\theta)}{\int f_L(C|\theta') f_{\text{pri}}(\theta') d\theta'} \quad (5)$$

314 where  $f_{\text{pri}}$  is the prior distribution (probability density) of the model parameters,  $f_L(C|\theta)$  is the likelihood function of the  
 315 model,  $C$  represents the observed compound concentrations, or  $\delta^{15}\text{N}$  values, and  $\theta$  denotes the model parameters. The

316 likelihood function  $f_L(C|\theta)$  is defined as a multivariate, uncorrelated Normal distribution with constant variances (standard  
317 deviation,  $\sigma_\delta$ ) for  $\delta^{15}\text{N}$  values, and variances increasing linearly with concentration, leading to a standard deviation  $\sigma_C =$   
318  $\sqrt{\sigma_{C,a}^2 C + \sigma_{C,b}^2}$  for  $\text{O}_2$ ,  $\text{SO}_4^{2-}$ , and N compound concentrations. This formulation incorporates the combined uncertainties in  
319 model structure, sampling, and concentration measurements. To account for the unknown magnitude of these uncertainties,  
320 the coefficients of these relationships,  $\sigma_{C,a}$ ,  $\sigma_{C,b}$ , and  $\sigma_\delta$  were inferred alongside the model parameters.

321 The marginal posteriors of individual parameters were compared with their priors to evaluate whether observational data  
322 provided information about these parameters, and whether this information was in conflict with the priors. In addition, two-  
323 dimensional marginals were examined to identify potential identifiability issues. Finally, uncertainty in the model results was  
324 calculated by propagating parameter uncertainty to the model results under consideration of their uncertainty for given  
325 parameter values as formulated in the likelihood function:

$$326 \quad f_{\text{post}}(C) = \int f_L(C|\theta) f_{\text{post}}(\theta) d\theta \quad (6)$$

327 For the parameters with marginal posteriors in conflict with prior information, we conducted additional scenario analyses,  
328 fixing parameters, and narrowing or widening prior distributions. These analyses evaluated the model's compatibility with  
329 observational data if parameters better aligned with prior information and assessed changes in posterior distribution with  
330 weaker priors. These scenario analyses complemented the assessment of bioturbation uncertainty mentioned above.

### 331 2.6 Discretization and numerical algorithms

332 The partial differential equations outlined in Appendix B: *Reaction-diffusion model* were solved using the Method of Lines.  
333 For spatial discretization, a grid was employed with cell thickness increasing progressively from the sediment surface toward  
334 deeper layers. This adaptive grid design reduced the total number of cells required, while still maintaining high resolution  
335 near the sediment-water interface, where steep concentration gradients typically occur (Appendix D: *Model discretization*).  
336 The resulting system of ordinary differential equations (ODE) was solved by a standard ODE solver. Parameter inference  
337 was conducted using two advanced Bayesian inference algorithms: Metropolis (Andrieu et al., 2003; Vihola, 2012) and  
338 Hamiltonian Monte Carlo (Betancourt, 2017; Neal, 2011) algorithms.

### 339 2.7 Model implementation

340 The model was implemented in Julia (Bezanson et al., 2017) (<https://julialang.org>) to achieve high-performance and  
341 facilitate automatic differentiation. The DifferentialEquations.jl package (Rackauckas and Nie, 2017) was used to solve the  
342 system of ODEs; performance testing of several ODE solvers identified the FBDF solver (adaptive order and adaptive time-  
343 step backward-differencing solver) as the most suitable for handling the stiffness of the ODE system. The ForwardDiff.jl  
344 package (Revels et al., 2016) was used for automatic differentiation; Bayesian inference was conducted using the adaptive  
345 Metropolis sampler from the AdaptiveMCMC package (Vihola, 2020), and the Hamiltonian Monte Carlo algorithm  
346 implemented in the AdvancedHMC.jl package (Xu et al., 2020). Further implementation details are provided in Appendix E:

347 *Model implementation.* Simulations were performed at sciCORE (<https://scicore.unibas.ch>), the scientific computing centre  
348 at the University of Basel.

349 **3. Sample collection and analyses**

350 **3.1 DIN concentrations and isotopes**

351 Sediment cores were retrieved at the deepest location of the Kreuztrichter basin in Lake Lucerne, a large oligotrophic lake in  
352 Switzerland (Baumann et al., 2024), in April 2021 using a gravity corer with PVC liners. The sediment cores were stored at  
353 4 °C and processed using two porewater-sampling methods: whole-core squeezing (WCS; (Bender et al., 1987)) for  $\text{NO}_3^-$   
354 samples, and Rhizon samplers (Rhizosphere research products, Wageningen, NL) for  $\text{NH}_4^+$  samples. The WCS technique  
355 provides a high depth resolution near the sediment-water interface (0-5 cm, resolution: ~ 0.7-1 mm), where  $\text{NO}_3^-$  is present  
356 in porewaters, while the Rhizon sampling method allows collecting samples at greater sediment depths (> 5 cm, resolution: ≥  
357 0.5 cm).  $\text{NO}_3^-$  and  $\text{NH}_4^+$  concentrations were measured using ion chromatography (940 Professional IC Vario, Metrohm).  
358  $\delta^{15}\text{N-NO}_3^-$  and  $\delta^{15}\text{N-NH}_4^+$  were determined using the denitrifier method (Casciotti et al., 2002; Sigman et al., 2001), and the  
359 hypobromite-azide method (Zhang et al., 2007), respectively. In both methods, sample N from  $\text{NO}_3^-$  or  $\text{NH}_4^+$  is converted  
360 into  $\text{N}_2\text{O}$ , which is then purified and analysed by isotope ratio mass spectrometry (Delta V Plus, Thermo Fisher Scientific).  
361 The typical analytical precision is ~ 0.25‰ (McIlvin and Casciotti, 2010).

362 **3.2 Process rate measurements**

363 For model parameterization, reaction rates for denitrification, DNRA, and anammox were determined using established  
364 protocols for  $^{15}\text{N}$ -tracer incubations (Holtappels et al., 2011). After recovery and sectioning of the core into 1-cm intervals, 1  
365 g of sediment was placed into 12 mL gas-tight glass vials (Exetainers®, Labo, UK). These Exetainers were then filled with  
366 anoxic, sterilized bottom water, amended with the following tracers: (Exp1)  $^{15}\text{NO}_3^-$ , (Exp2)  $^{15}\text{NH}_4^+ + ^{14}\text{NO}_2^-$ . Exetainers were  
367 incubated at 6 °C in the dark, and terminated at designated time points (0, 6, 12, 24, and 36 hours) by adding  $\text{ZnCl}_2$ . Gas  
368 headspace samples were analysed for the production of  $^{14}\text{N}^{15}\text{N}$  and  $^{15}\text{N}^{15}\text{N}$  using gas-chromatography isotope ratio mass  
369 spectrometry (GC-IRMS; Isoprime, Manchester, UK). Linear regression of  $^{14}\text{N}^{15}\text{N}$  and  $^{15}\text{N}^{15}\text{N}$  production over time was  
370 used to calculate  $\text{N}_2$  production rates, with standard errors derived from deviations in the regression slopes across the five-  
371 time points. For the determination of  $^{15}\text{NH}_4^+$  production from  $^{15}\text{NO}_3^-$  additions,  $^{15}\text{NH}_4^+$  was chemically converted to  $\text{N}_2$  gas  
372 using the alkaline-hypobromite method (Jensen et al., 2011). The resulting  $^{14}\text{N}^{15}\text{N}$  was quantified by GC-IRMS. Linear  
373 regression of  $^{14}\text{N}^{15}\text{N}$  production over time was used to calculate potential rates of  $^{29}\text{N}_2$  (i.e.,  $^{15}\text{NH}_4^+$ ) production. Rates of  
374 denitrification, DNRA, and anammox were calculated according to Holtappels et al. (2011) and Risgaard-Petersen et al.  
375 (2003). Only data from the upper 1 cm were used to parameterize the model, as the investigated sediments displayed a  
376 shallow nitracline and the highest anammox contribution at 0-0.5 cm depth.

377 **4. Results and Discussion**

378 The developed diagenetic N isotope model addresses existing knowledge gaps in understanding porewater N dynamics, and  
379 aims to clarify the roles of distinct N-transformation processes in shaping the distribution of N isotopes to be potentially used  
380 to constrain benthic N (isotope) fluxes across different environments. Here, we present (1) the results of Bayesian inference  
381 applied to a large number (~ 60) of model parameters (see prior definition in Appendix C: *Prior values for inference*), with a  
382 focus on assessing their uncertainty, (2) a detailed scenario analysis, focusing on parameters that exhibit significant shifts in  
383 their marginal posterior distributions relative to their prior, as well as on the effect of variable contributions from different  
384  $\text{NO}_3^-$  and  $\text{NO}_2^-$  reduction pathways, and the impact of enhanced bioturbation on model outcomes, (3) a sensitivity analysis,  
385 evaluating the importance of individual model processes in shaping benthic N isotope dynamics, (4) the importance of  
386 process coupling in benthic N cycling, with a particular focus on the role of intermediate  $\text{NO}_2^-$  in influencing  $\delta^{15}\text{N}$ - $\text{NO}_3^-$   
387 dynamics. All results are based on porewater concentration, isotope, and rate measurement data from a sampling campaign  
388 conducted in Lake Lucerne in April 2021. Additionally, we performed (5) a sensitivity analysis examining model output  
389 responses to modifications of selected parameters using artificially simulated settings (e.g., variable contributions of  
390 denitrification/anammox/DNRA); this analysis demonstrates the model's capability for addressing diverse research  
391 questions.

392 **4.1 Bayesian inference**

393 The model implementation was highly efficient, achieving simulation times of about 12 s on an 13th Gen Intel® Core™ i9-  
394 13,900K processor with 3.00 GHz and 64 GB of memory (of which only a small fraction was needed) for a 100-day  
395 simulation starting from constant concentration profiles. This efficiency enabled the execution of Markov chains of 20,000  
396 iterations within a few days on the scientific computing centre at the University of Basel (<https://scicore.unibas.ch>). By  
397 combining these chains, samples of 100,000 iterations were generated. The Hamiltonian Monte Carlo algorithm  
398 outperformed the adaptive Metropolis algorithm during burn-in to the core of the posterior distribution. However, for final  
399 posterior sampling with about 60 parameters, adaptive Metropolis sampling proved more efficient in terms of effective  
400 sample size per unit of simulation time. Despite these efforts in getting computational efficiency, and the use of advanced  
401 MCMC algorithms, reaching convergence of the Markov chains remained challenging. We got five consistent Markov  
402 chains without discernible trends for each scenario; however, some widening of the chains and the resulting effective sample  
403 size on the order of 500 indicate that we are not able to get a good coverage of the tails of the posterior distribution. This  
404 outcome demonstrates that incorporating so many uncertain model parameters pushes the limits of Bayesian inference in  
405 terms of numerical tractability. However, the resulting uncertainty estimates are certainly more realistic than those obtained  
406 by fixing many poorly constrained parameters to unique values to reduce the dimension of the parameter space.  
407 The simulation results of solute concentration and  $\delta^{15}\text{N}$  profiles in the most plausible Base scenario (Fig. 2) integrate prior  
408 knowledge (Appendix C: *Prior values for inference*) with observational data through Bayesian inference. The profiles

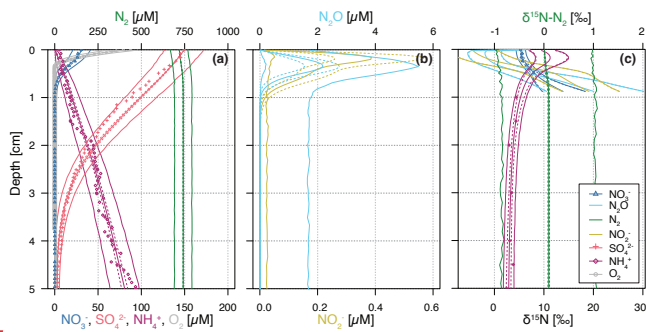
409 closely reproduce the available, albeit limited, data, and conform to expected depth-related trends: oxidants (i.e., O<sub>2</sub>, NO<sub>3</sub><sup>-</sup> and SO<sub>4</sub><sup>2-</sup>) are readily consumed via aerobic mineralization and nitrification (O<sub>2</sub>), denitrification (NO<sub>3</sub><sup>-</sup>), and SO<sub>4</sub><sup>2-</sup> reduction. 410 While mineralization is assumed to involve negligible N isotopic fractionation, the first step of nitrification causes 411 significant enrichment in <sup>15</sup>N of the residual NH<sub>4</sub><sup>+</sup> pool, yielding  $\delta^{15}\text{N-NH}_4^+$  values up to 11.2‰ at 0.15 cm, due to strong N 412 isotope fractionation, estimated at  $\varepsilon_{\text{Nitr}}$  = 12.0‰ (to NO<sub>2</sub><sup>-</sup>) and 36.4‰ (to N<sub>2</sub>O). Unfortunately, extremely low NH<sub>4</sub><sup>+</sup> 413 concentrations measured in the top 2 cm hindered the determination and verification of the modelled  $\delta^{15}\text{N-NH}_4^+$  in this zone 414 with field data. Both NO<sub>2</sub><sup>-</sup> and N<sub>2</sub>O accumulate in the upper 0.5 cm, reaching up to 0.4  $\mu\text{M}$  and 2  $\mu\text{M}$ , respectively. Below 415 0.3 cm, denitrification leads to the progressive <sup>15</sup>N enrichment of NO<sub>3</sub><sup>-</sup>, NO<sub>2</sub><sup>-</sup> and N<sub>2</sub>O, while N<sub>2</sub>-producing mechanisms (i.e., 416 denitrification and anammox) cause only minimal changes to the modelled  $\delta^{15}\text{N-N}_2$  profile, due to the dominance of a large 417 pre-existing N<sub>2</sub> pool. For concentrations, the 95% credibility intervals of parametric uncertainty are rather narrow, whereas 418 the much broader total uncertainty is dominated by the lumped uncertainty term in the likelihood function, which primarily 419 reflects the model's structural uncertainty. The error, beyond the parameter error, is parameterized using the two sigma 420 values ( $\sigma_{\text{C},a}$  and  $\sigma_{\text{C},b}$ ; see Sect. 2.5), and exceeds what would arise from measurement and sampling alone. This suggests that 421 the larger error is attributable to the model's structural limitations. Conversely,  $\delta^{15}\text{N}$  profiles exhibit small total uncertainty, 422 as model results for  $\delta^{15}\text{N}$  closely match observational data, with minimal random and systematic deviations (parameterized 423 using the sigma value  $\sigma_{\delta}$ , see Sect. 2.5).

424 The model provides insights into the underlying process rates (Fig. 3) that shape the simulated profiles (Fig. 2). Vertical 425 profiles of transformation rates for NH<sub>4</sub><sup>+</sup>, NO<sub>3</sub><sup>-</sup>, NO<sub>2</sub><sup>-</sup> and N<sub>2</sub>O clearly illustrate the sequential dominance of different N- 426 transformation processes with increasing sediment depth and decreasing O<sub>2</sub> availability. Aerobic processes, namely aerobic 427 mineralization and nitrification, primarily control NH<sub>4</sub><sup>+</sup> transformation rates, peaking at 450 and 350  $\mu\text{M d}^{-1}$ , respectively 428 (Fig. 3a). Nitrification sustains denitrification by producing both NO<sub>2</sub><sup>-</sup> (up to 350  $\mu\text{M d}^{-1}$ ) and NO<sub>3</sub><sup>-</sup> (up to 275  $\mu\text{M d}^{-1}$ ) in the 429 upper 0.4 cm (Fig. 3b-c). A strong spatial overlap of nitrification and denitrification emerges in the depth distribution of 430 processes affecting the NO<sub>2</sub><sup>-</sup> pool, suggesting a potential interplay between these pathways (Fig. 3c).

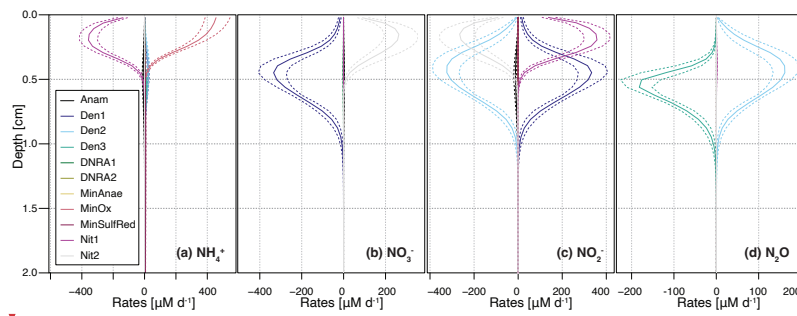
431 A key strength of this model is the incorporation of N<sub>2</sub>O as a state variable. Our model results reveal that, although N<sub>2</sub>O 432 production via nitrification is minimal (not visible in Fig. 3d), the strong isotopic fractionation associated with this reaction 433 ( $\varepsilon_{\text{Nitr},\text{N}_2\text{O}} = 36.4\text{‰}$ ) generates N<sub>2</sub>O with  $\delta^{15}\text{N}$  values of -1.2‰ to -2.2‰ in the top 0.2 cm (Fig. 2c). At a depth of 434 approximately 0.35 cm, up to 2.1  $\mu\text{M}$  of N<sub>2</sub>O accumulate, coinciding with the highest rates of N<sub>2</sub>O production through 435 denitrification. Conversely, N<sub>2</sub>O consumption by the last denitrification step peaks at 0.5 cm, leading to a progressive 436 increase in  $\delta^{15}\text{N-N}_2\text{O}$  with depth. This zonation likely reflects the O<sub>2</sub> sensitivity of the distinct N<sub>2</sub>O-producing and - 437 consuming processes. Specifically, N<sub>2</sub>O reductases are known to be strongly inhibited by O<sub>2</sub>, and therefore exhibit greater 438 activity below the oxycline (Wenk et al., 2016). Although the model does not explicitly include the enzymes responsible for 439 N-transformation pathways, the chosen and estimated kinetic parameters reflect substrate affinity and inhibition strength. 440

441 Consequently, inhibition constants like  $K_{O2,Den2}$  and  $K_{O2,Den3}$  provide indirect insights into the  $O_2$  dependency of these  
442 enzyme-mediated reactions, effectively shaping the modelled redox zonation.

443 The model adequately captures the concentration and isotopic composition of the state variables, in agreement with field  
444 measurement and the expected patterns of underlying N-transformation processes and reaction coupling (Fig. 2 and 3). One  
445 key strength of the step-wise model is its ability to quantify reaction coupling, which is challenging to infer directly from  
446 state variable pools (i.e., reactive intermediates), if they are rapidly turned over.



447  
448 **Figure 2.** Vertical porewater profiles of concentrations (a-b) and isotopic composition ( $\delta^{15}\text{N}$ ) (c) of the state variables for the Base  
449 scenario. Continuous lines represent model simulations, while symbols represent observational data from Lake Lucerne. For  $\text{NH}_4^+$   
450 concentrations, filled diamonds represent low-resolution data from Rhizon sampling, while open diamonds represent the high-  
451 resolution WCS data, adjusted to align with absolute concentrations measured in the low-resolution dataset. Dashed lines enclose  
452 95% credibility intervals resulting from parametric uncertainty, while thin solid lines represent total uncertainty.



453  
454 **Figure 3.** Vertical profiles of transformation rates for distinct N-cycling processes affecting the  $\text{NH}_4^+$ ,  $\text{NO}_3^-$ ,  $\text{NO}_2^-$ , and  $\text{N}_2\text{O}$  pools.  
455 Dashed lines enclose 95% credibility intervals resulting from parametric uncertainty. Positive reaction rate values indicate  
456 production, negative values indicate consumption of a given DIN species.

457 To address the variable ranges for the model parameters found in the literature, and to reduce structural uncertainty imposed  
458 by fixed parameter values, we estimated a large set of parameters using Bayesian inference. The obtained joint posterior

461 distribution of model parameters enabled us to assess the knowledge acquired from data. Marginal posterior distributions of  
462 individual parameters, and two-dimensional marginal distributions of parameter pairs, were particularly useful in this context  
463 (Fig. 4 shows examples for the four categories defined below; Fig. S1 provides an overview of all marginal prior and  
464 posterior parameter distributions). By comparing marginal posterior distributions with their corresponding priors, parameters  
465 were classified as well identifiable or poorly identifiable. While this classification involves some subjectivity in determining  
466 how much narrower a posterior distribution should be compared to its prior distribution to classify such parameter as well  
467 identifiable, some clear patterns emerged:

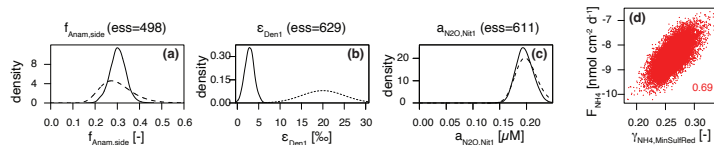
- 468 1. Well identifiable parameters: The marginal posterior distribution is clearly narrower than the prior, indicating that  
469 data provide meaningful information about the parameter's value. Two cases were observed:
  - 470 a. The marginal posterior distribution is within the prior range, suggesting that the information from the data is in  
471 agreement with prior knowledge (Fig. 4a). Examples include:  $f$  factors for anammox ( $f_{Anam,Den2} = 0.2$ ) and both  
472 DNRA steps ( $f_{DNRA1,Den1} = 0.005$ ,  $f_{DNRA2,Den2} = 0.005$ ), estimated using  $^{15}\text{N}$ -tracer incubation experiments for the  
473 investigated system, and parameters such as  $K_{NO3,Den1}$  and  $K_{O2,MinOx}$ , constrained from clearly defined oxidant  
474 declines. Maximum conversion rates for aerobic mineralization, denitrification,  $\text{SO}_4^{2-}$  reduction, and anaerobic  
475 mineralization, as well as the  $\text{NH}_4^+$  flux from deeper sediment layers, also belong to this category, although we  
476 approximated very wide priors by uniform priors (see Sect. 2.4), making it less visible in the plot.
  - 477 b. The marginal posterior distribution significantly deviated from the prior range (Fig. 4b), suggesting that the  
478 information from the data is in conflict with prior knowledge. The most striking example is  $\varepsilon_{Den1}$ , estimated at  
479  $2.8 \pm 1.1\%$  for the Lake Lucerne dataset, far lower than the typical 15–25% reported in the literature for  $\text{NO}_3^-$   
480 reduction (Lehmann et al., 2003; Rooze and Meile, 2016), suggesting a reduced N-isotopic fractionation (or at  
481 least, of its expression) at the porewater level. This finding contrasts with model-derived values for the cellular  
482 isotope effect of  $\text{NO}_3^-$  reduction observed in the porewater of marine sediments ( $\varepsilon_{Den} > 10\%$ ) (Lehmann et al.,  
483 2007). While a detailed investigation of the biological mechanisms behind such reduced expression across  
484 benthic environments is beyond the scope of this study and will be addressed separately by the authors, the  
485 potential role of reaction couplings in modulating benthic N isotope dynamics is discussed in Section 4.4.
- 486 2. Poorly identifiable parameters: The marginal posterior distribution resembles the prior distribution, suggesting poor  
487 identifiability. This can occur for two possible reasons:
  - 488 a. The parameter exerts negligible influence on the model output that corresponds to observational data (Fig. 4c).  
489 For example, parameters like the  $\text{N}_2\text{O}$  yield during nitrification,  $a_{N2O,Nit1}$  and  $b_{N2O,Nit1}$ , could not be constrained  
490 without specific data on  $\text{N}_2\text{O}$  production. The current model encompasses several processes and state variables,  
491 which, at times, were hard to corroborate with the limited dataset in hand (a situation that may apply regularly  
492 to environmental studies, particularly in benthic environments). Therefore, their values were taken from  
493 previous studies (Ji et al., 2018). For other parameters, such as  $\gamma_{NH4,DNRA1}$  and  $\gamma_{NH4,DNRA2}$ , little knowledge was

494 acquired from the data in hand, due to the relatively low maximum rates of DNRA compared to other  
 495 processes. In such cases, the posterior distribution may remain close to the prior, not because the prior range  
 496 was incorrect, but because the available data could not further constrain it.

497 b. Although data are available and the model output is sensitive to the parameter, other parameters influence the  
 498 output similarly. This leads to parameter correlation in the posterior distribution and reduces identifiability, as  
 499 observed for  $\gamma_{NH4,MinSulfRed}$  and  $F_{NH4}$  (Fig. 4d), which exhibit correlation, making their estimates interdependent  
 500 (Guillaume et al., 2019). Here, the estimate of the  $NH_4^+$  flux from the lower boundary of the model depends on  
 501 the estimate of the amount of  $NH_4^+$  released via OM mineralization coupled to  $SO_4^{2-}$  reduction.

502 The comparison of marginal priors and posteriors of the parameters (Fig. S1) demonstrates that excellent agreement between  
 503 model outputs and observational data (Fig. 2) can be achieved for 54 of the 58 estimated parameters compatible with their  
 504 priors. Exceptions include: the higher-than-expected rate for the second denitrification step relative to the first (expressed by  
 505 the factor  $f_{Den2,Den1}$ ), the large half-saturation constant for  $SO_4^{2-}$  reduction ( $K_{SO4,MinSulfRed}$ ), and smaller-than-expected N  
 506 isotope effects for the first steps of denitrification and nitrification ( $\varepsilon_{Den1}$  and  $\varepsilon_{Nitr,NO2}$ , respectively). The largest deviation is  
 507 observed for  $\varepsilon_{Den1}$ , which is further examined in the next subsection.

508 Notably, the seven parameters, for which a uniform prior was chosen to approximate a very wide prior ( $k_{MinOx}$ ,  $k_{Den1}$ ,  
 509  $k_{MinSulfRed}$ ,  $k_{MinAnae}$ ,  $k_{Nitr1}$ ,  $F_{NH4}$ ,  $\delta^15N_{NH4}$ ), were identifiable, indicating that highly system-specific prior knowledge is not  
 510 crucial for these estimates. Most of the other model parameters showed limited narrowing of the marginal posterior relative  
 511 to the prior, reflecting the rather limited information gain that can be obtained from data. The three model error parameters  
 512 ( $\sigma_{C,a}$ ,  $\sigma_{C,b}$ ,  $\sigma_0$ ) were well identifiable and will be used in the following sections to compare the fit quality across different  
 513 modelling scenarios.



514  
 515 **Figure 4. Prior (dashed line) and posterior marginal distributions (continuous line) for illustrative parameters, which could be**  
 516 **identified and showed (a) good ( $f_{Anam.side}$ ) and (b) poor agreement ( $\varepsilon_{Den1}$ ) with prior knowledge, and (c) for parameters, that could**  
 517 **not be identified ( $a_{N2O,Nitr}$ ); 2D correlation plot for  $\gamma_{NH4,MinSulfRed}$  versus  $F_{NH4}$  (d).**

#### 518 4.2 Scenario analysis

519 Building on the findings discussed in the previous subsection, we explored the apparent prior-data conflict regarding  $\varepsilon_{Den1}$  in  
 520 greater detail. Additionally, we assessed whether the estimated process rates overlooked potential reaction coupling, which  
 521 might go undetected through  $^{15}N$ -tracer incubation experiments, by exploring the variability in contributions of anammox

522 and DNRA (i.e.,  $f_{Anam}$ ,  $f_{DNRA1}$  and  $f_{DNRA2}$ ). Lastly, given the uncertainty regarding solute-diffusion enhancement by  
523 bioturbation, we investigated a scenario with increased bioturbation. These considerations led to four key scenarios:

524 A. *Narrow priors for  $\varepsilon$ .* This scenario investigated the effects of restricting  $\varepsilon$  variability to a narrower range (prior  
525 standard deviation of 1% instead of 5%). The aim was to test whether the marked reduction in the marginal  
526 posterior of  $\varepsilon_{Denl}$  persisted under stricter prior assumptions, and whether this decreased flexibility significantly  
527 impacted the quality of the model fit.

528 B. *Fixed  $\varepsilon$ .* Here, the model output was assessed under the assumption that the literature data regarding N isotope  
529 effects are correct (i.e.,  $\varepsilon$  values not estimated). This scenario complemented Scenario A by testing whether a good  
530 fit to the data could still be achieved by fixing the  $\varepsilon_{Denl}$  value (and all other isotope effects) at its prior mean.

531 C. *Wider priors for  $f$ .* In this scenario, greater variability in DNRA and anammox contributions (prior standard  
532 deviation of 100% instead of 25%) was allowed to test the impact of relaxed prior assumptions on the relative  
533 contributions of these processes in the model output.

534 D. *Enhanced bioturbation.* This scenario simulated a faster solute-diffusive transport due to higher infaunal activity by  
535 doubling the bioturbation coefficient ( $D_{bio} = 2 \text{ cm}^2 \text{ d}^{-1}$  instead of  $1 \text{ cm}^2 \text{ d}^{-1}$ ), to investigate the sensitivity of the  
536 results to this uncertain parameter, which was not included in the Bayesian analysis. In the model, the bioturbation  
537 strength at the sediment surface is defined by the parameter  $D_{bio}$ , and it decreases exponentially with depth, with the  
538 typical bioturbation depth parameter,  $depth_{bio}$ . As the diffusion enhancement by bioturbation is highly uncertain,  
539 this scenario aims to assess solely the sensitivity of the model output to changing bioturbation magnitude.

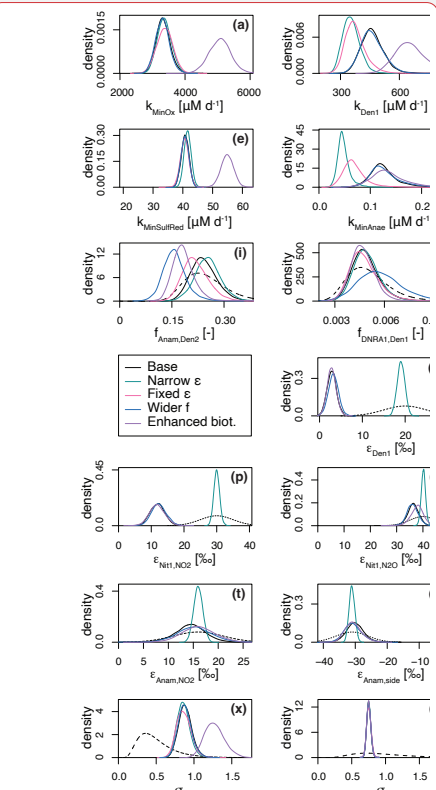
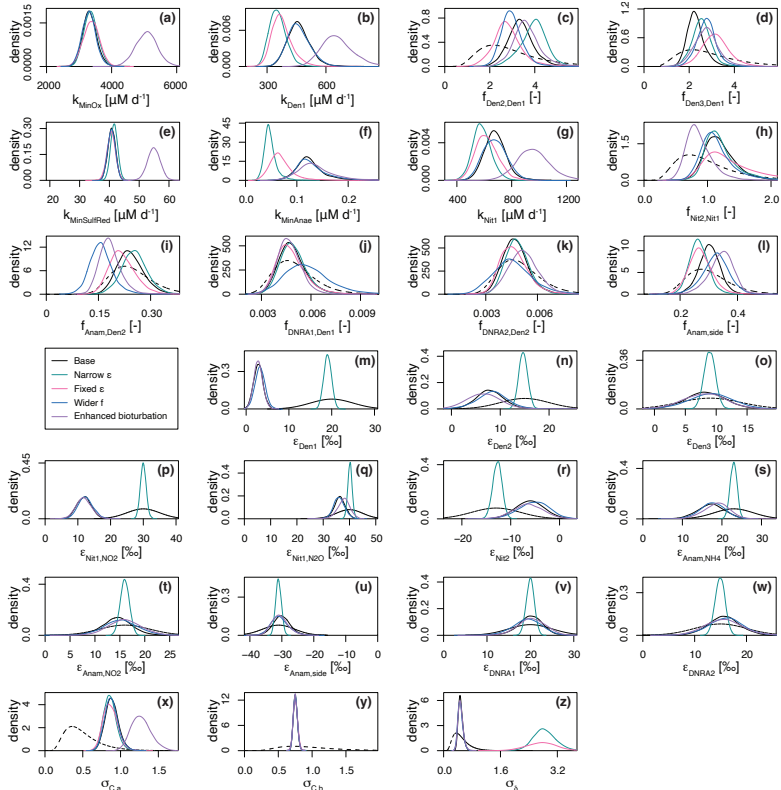
540 The results demonstrate a strong dependence of the estimated parameters on the chosen prior assumptions (Fig. 5). Across all  
541 scenarios, marginal posterior distributions for the selected parameters are generally narrower than the prior distributions,  
542 though results vary substantially. In Scenario A (*Narrow priors for  $\varepsilon$* ), restricting the prior range significantly constrained  
543  $\varepsilon_{Denl}$ , limiting its deviation from the prior (Fig. 5m; note that the prior for Scenario A is five times narrower than the one  
544 shown, which represents the prior for all other scenarios). These results closely resemble those from Scenario B (*Fixed  $\varepsilon$* ),  
545 where no deviation was possible (Fig. 5, Fig. S2). Both scenarios exhibit lower denitrification rates than the Base scenario  
546 (Fig. 5b), but comparable fit quality for total ( $^{14}\text{N} + ^{15}\text{N}$ ) concentration, quantified by  $\sigma_{C,a}$  (i.e., the dominant term of standard  
547 deviation of the model error for concentrations, see Sect. 2.5) (Fig. 5x). On the other hand, Scenarios A and B display poorer  
548 fit quality for  $\delta^{15}\text{N}$  profiles, indicated by a large value of  $\sigma_\delta$  (Fig. 5z), suggesting that the model structure cannot adequately  
549 reproduce the  $\delta^{15}\text{N-NO}_3^-$  profiles without adapting the  $\varepsilon_{Denl}$  value. While biological isotope effects of 15–30‰ are typical for  
550  $\text{NO}_3^-$  reduction (Lehmann et al., 2007), lower values under almost-complete  $\text{NO}_3^-$  consumption have been reported (Thunell  
551 et al., 2004; Wenk et al., 2014). This finding is further confirmed by comparable marginal posteriors for  $\varepsilon_{Denl}$  across all  
552 scenarios considered in this study, besides scenarios A and B. To test the robustness of our model, we ran a base scenario  
553 simulation for marine sediments in the Bering Sea (station MC16) (Lehmann et al., 2007) (data not shown). Moreover, a

554 [manuscript currently in preparation presents an extensive comparison of model application across different sites and](#)  
555 [demonstrates a much wider range of  \$\delta^{15}\text{N}\_{\text{Den1}}\$  values, exceeding 20‰.](#)

556 In Scenario C (*Wider f*), allowing greater variability in anammox and DNRA contributions results in the lowest  $f_{\text{Anam},\text{Den2}}$   
557 values, although such deviation is not substantial compared to the Base scenario output (Fig. 5i). The estimated  $f_{\text{DNRA1},\text{Den1}}$   
558 and  $f_{\text{DNRA2},\text{Den2}}$  values in Scenario C mostly align with those of the Base scenario, corroborating the marginal role of DNRA  
559 in Lake Lucerne. Such findings confirm the accuracy of the rate measurements performed with  $^{15}\text{N}$  tracer incubations.

560 Scenario D (*Enhanced bioturbation*) stands out with the highest conversion rates (i.e.,  $k_{\text{MinOx}}$ ,  $k_{\text{MinSulfRed}}$ , and  $k_{\text{Nit1}}$ ) (Fig. 5a,e,g)  
561 to ensure sufficient oxidant consumption at higher supply/flux rates (reproducing the observed gradient despite higher  
562 diffusivity). Despite these changes, bioturbation had negligible effects on porewater N isotope dynamics, with estimated  
563 isotope effects and fit quality for  $\delta^{15}\text{N}$  profiles ( $\sigma_{\delta}$ ) comparable to those of the Base scenario.

564 The obtained concentration depth profiles for the four scenarios are generally comparable, as newly estimated parameters  
565 ensured good fitting of the data (Fig. S2). However, in Scenarios A and B, stricter constraints on prior knowledge for  
566 parameter estimation result in little to no suppression of all isotope effects (i.e., relatively strong N isotopic fractionation),  
567 leading to great variability in the  $\delta^{15}\text{N}$  profiles. Poor fits to the  $\delta^{15}\text{N}$  data are observed under these conditions, as evidenced  
568 by the greater  $^{15}\text{N}$  enrichment of the  $\text{NO}_3^-$  pool compared to the measured-data profiles (Fig. S2). Similarly, the  $\delta^{15}\text{N}-\text{N}_2\text{O}$   
569 profiles exhibit sharp declines to approximately -15‰ in the upper 0.5 cm under Scenarios A and B, driven by the strong  
570 expression of  $\epsilon_{\text{Nit1},\text{N}_2\text{O}}$  (40.1‰ and 40.0‰, respectively). In contrast, Scenarios C and D closely resemble the Base scenario,  
571 with only minor  $\delta^{15}\text{N}-\text{N}_2\text{O}$  variations.



572

573 **Figure 5.** Marginal probability densities across the five considered scenarios for selected estimated parameters, showing both prior  
 574 and posterior distributions (continuous lines): *Base scenario* ( $SD_f = 25\%$ ,  $SD_\epsilon = 5\%$ ,  $D_{bio} = 1 \text{ cm}^2 \text{ d}^{-1}$ ), *Narrower  $\epsilon$*  ( $SD_\epsilon = 1\%$ ),  
 575 *Fixed  $\epsilon$*  (i.e.,  $\epsilon$  taken from bibliography), *Wider  $f$*  ( $SD_f = 100\%$ ) and *Enhanced bioturbation* ( $D_{bio} = 2.0 \text{ cm}^2 \text{ d}^{-1}$ ). Of the ~60  
 576 estimated parameters, those shown here were selected for their relevance to the discussion. See main text for further details.

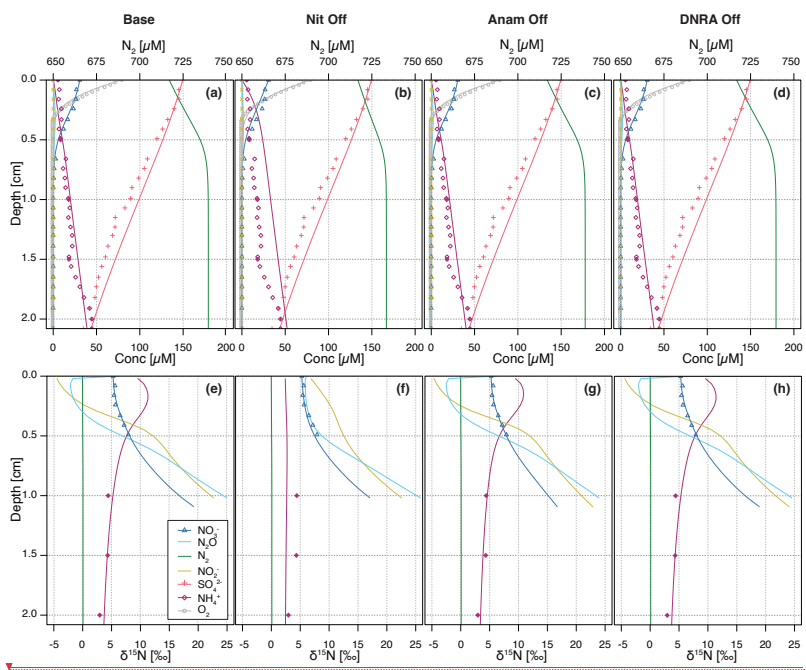
#### 577 4.3 Importance of modelled processes and their impact on porewater N isotope signatures

578 The importance of modelled processes and their impact on N isotope signatures were investigated by selectively deactivating  
 579 individual processes and comparing the model outputs to the Base scenario. Aerobic mineralization, denitrification, and  
 580  $\text{SO}_4^{2-}$  reduction were considered essential to preserve redox zonation (e.g., sequential decline of  $\text{O}_2$ ,  $\text{NO}_3^-$ , and  $\text{SO}_4^{2-}$ ) and N  
 581 dynamics. The following processes were individually turned off: (a) nitrification (“NitOff”); (b) anammox (“AnamOff”);  
 582 and (c) DNRA (“DNRAOff”). Initially, each process was simply inactivated to assess its impact on model outputs (Fig. 6).

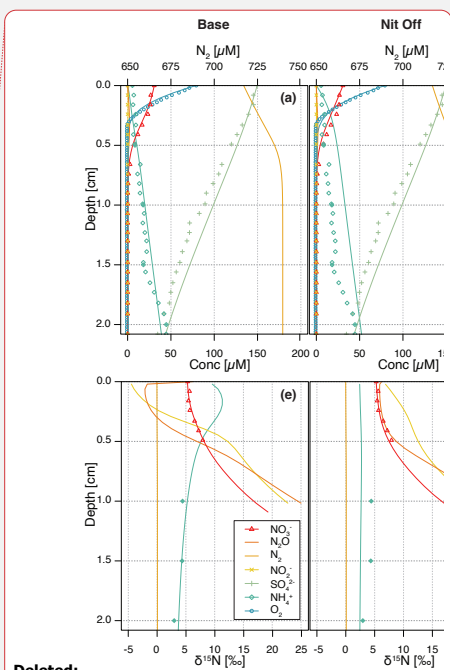
584 Subsequently, inference was conducted after deactivating each process, to investigate their importance for model  
585 performance, parameter and flux estimation, and for the identifiability of rate parameters by evaluating the quality of the fit  
586 to the data, especially on the  $\delta^{15}\text{N}$  profiles (Fig. 7, Fig. S3, Fig. S4).

587 Switching off nitrification significantly alters the model output compared to the Base scenario (Fig. 6a-b,e-f), indicating its  
588 central role in the benthic N dynamics. Key effects include  $\text{NH}_4^+$  accumulation throughout the investigated depths, with a  
589 flattening of the  $\delta^{15}\text{N}-\text{NH}_4^+$  profile (i.e., less curvature towards higher  $\delta^{15}\text{N}$  values) in the upper 0.5 cm, as the only other  
590 source of  $^{15}\text{N}$ -enriched  $\text{NH}_4^+$  besides nitrification would be anammox, which is inhibited under oxic conditions. Furthermore,  
591 nitrification-denitrification coupling via  $\text{NO}_2^-$  weakens in this scenario, resulting in lower overall  $\text{N}_2$  production (as indicated  
592 by the lower maximum  $\text{N}_2$  concentration of 734  $\mu\text{M}$  compared to 745  $\mu\text{M}$  in the Base scenario). These results suggest that  
593 partially reducing, or fully eliminating, nitrification lowers the system's capacity to act as an efficient N sink. In other words,  
594 the findings confirm that nitrification is a critical process that, when closely coupled to denitrification, helps to enhance the  
595 ecosystem's potential to remove fixed N. All other N-isotopic state variables also show a flatter  $\delta^{15}\text{N}$  profile, with only a  
596 progressive enrichment in  $^{15}\text{N}$  below 0.5 cm, primarily driven by denitrification ( $\text{NO}_3^-$ ,  $\text{NO}_2^-$ , and  $\text{N}_2\text{O}$ ). The impact of  
597 disabling nitrification is clearly reflected in the  $\delta^{15}\text{N}-\text{N}_2\text{O}$  profile across the upper 0.3 cm, where the typical nitrification-  
598 induced dip is absent, and  $\delta^{15}\text{N}-\text{N}_2\text{O}$  values remain relatively constant (~7-8%). In contrast, the effects of turning off  
599 anammox or DNRA are more subtle, owing to their generally lower reaction rates in Lake Lucerne (Fig. 6c-d,g-h). Notably,  
600 in the absence of anammox,  $\text{N}_2\text{O}$  exhibits lower  $\delta^{15}\text{N}$  values in the upper 0.3 cm compared to the Base scenario, likely due to  
601 higher  $\text{N}_2\text{O}$  yields via nitrification, as reduced competition for  $\text{NH}_4^+$  with anammox provides more substrate for nitrification.  
602 Upon running inference for each case, concentration and N isotope profiles for the NitOff, AnamOff, and DNRAOff  
603 scenarios are generally similar to those of the Base scenario (Fig. S3), with notable exceptions in the NitOff case. In the  
604 absence of nitrification,  $\text{NH}_4^+$  accumulates and the  $\delta^{15}\text{N}-\text{NH}_4^+$  profile remains largely flat, since anammox, the only other  
605  $\text{NH}_4^+$ -consuming process, is minimal under oxic conditions. No  $\delta^{15}\text{N}-\text{NH}_4^+$  measurements are available for the top 1 cm, so  
606 the model output could not be verified with field data. The  $\text{N}_2\text{O}$  pool systematics also diverge between the NitOff and Base  
607 scenarios. Specifically, in the NitOff case, no nitrification-derived  $\text{N}_2\text{O}$  accumulates in the upper 0.4 cm, and consequently,  
608 the  $\delta^{15}\text{N}-\text{N}_2\text{O}$  profiles lack the typical nitrification-associated decline in this layer. Instead,  $\text{N}_2\text{O}$  becomes progressively  
609 enriched in  $^{15}\text{N}$  below 0.4 cm. While most estimated parameters and fluxes are consistent across the four scenarios, the  
610 NitOff scenario stands out again, exhibiting strong effects on the anammox rates and associated isotope effects (e.g.,  
611  $f_{\text{Anam},\text{Den2}}$ ,  $\mathcal{E}_{\text{Anam},\text{NH}_4}$ ) (Fig. S4), as well as on benthic fluxes of  $\text{NH}_4^+$ ,  $\text{NO}_2^-$ ,  $\text{NO}_3^-$  and  $\text{N}_2\text{O}$  (Fig. 7). Nonetheless, the  $\text{NH}_4^+$   
612 concentration profile is well-captured, as indicated by a low  $\sigma_{C,a}$ , reflecting a good match between model and concentration  
613 data even in the absence of nitrification. This finding implies that the model cannot resolve the relative contributions of  
614 nitrification versus anammox to  $\text{NH}_4^+$  consumption based on the concentration and isotope data, highlighting the importance  
615 of prior knowledge regarding  $f_{\text{Anam},\text{Den2}}$ .

616 The comparison of process rates across these four scenarios provides insights, unveiling the extent of process coupling and  
 617 competition (Fig. S5) (Hines et al., 2012). For instance, anammox and nitrification compete for both  $\text{NH}_4^+$  and  $\text{NO}_2^-$  as  
 618 substrates, causing the rate of one process to be enhanced, when the other is switched off. For instance,  $\text{NH}_4^+$  oxidation and  
 619  $\text{NO}_2^-$  production rates via nitrification (Nit1) are higher ( $\sim 0.2$  cm depth) in the AnamOff scenario than in the Base scenario.  
 620 Even more obviously, enhanced rates of  $\text{NH}_4^+$  oxidation,  $\text{NO}_2^-$  consumption, and  $\text{NO}_3^-$  production via anammox are observed  
 621 in the NitOff scenario than in the Base scenario. Process coupling, specifically nitrification-denitrification, is further  
 622 confirmed by lower rates for  $\text{NO}_2^-$  reduction via denitrification (Den2) in the absence of nitrification. In general, the  
 623 influence of DNRA on production and consumption rates of the considered state variable appears minimal, owing to the  
 624 limited environmental relevance of DNRA in Lake Lucerne. Overall, the similarly good fits obtained across these three  
 625 scenarios and the *Base* scenario reflect the poor identifiability of the switched off processes; this suggests that the data can be  
 626 well-fitted even without these three processes, emphasizing the importance of prior knowledge about their environmental  
 627 relevance.

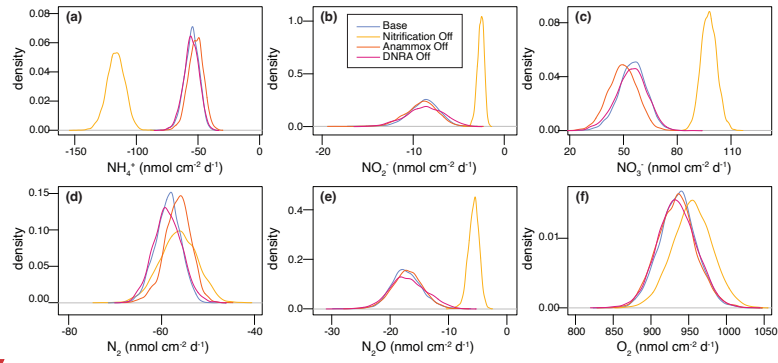


628  
 629 **Figure 6.** Vertical concentration (a-d) and isotopic composition (e-h) profiles for state variables. Model output obtained with all  
 630 processes included (a, e) are compared with model simulations where individual processes are switched off: nitrification (b, f),



Deleted:

632 anammox (c, g), and DNRA (d, h), without running inference again. Continuous lines represent the model output, while symbols  
 633 represent measured data from Lake Lucerne. For  $\text{NH}_4^+$ , open diamonds represent the high-resolution dataset, adjusted to align  
 634 with absolute concentrations measured in the low-resolution dataset (filled diamonds).

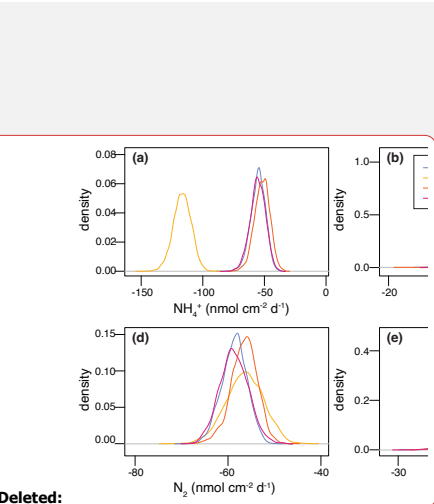


635  
 636 **Figure 7. Posterior marginal probability distributions of modelled sediment-water interface fluxes (in  $\text{nmol cm}^{-2} \text{ d}^{-1}$ ) for all state**  
 637 **variables, generated from inference runs, across the four scenarios considered for model validation against experimental data**  
 638 **from Lake Lucerne.**

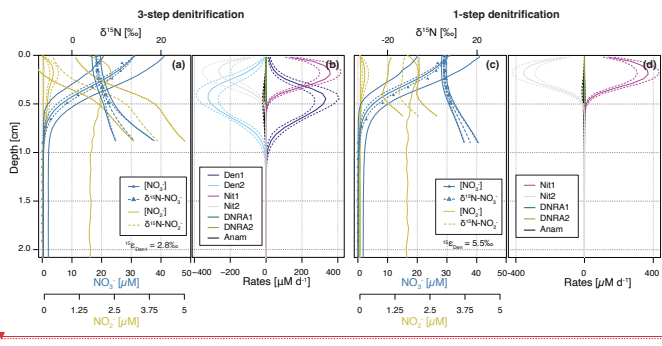
#### 639 4.4 The role of process coupling via $\text{NO}_2^-$

640 Previous models of benthic N isotope dynamics have focused on individual reactions or overlooked the role of intermediate  
 641 species, such as  $\text{NO}_2^-$  (Kessler et al., 2014; Lehmann et al., 2007). Our study confirms that  $\text{NO}_2^-$  plays a critical role in  
 642 coupling multiple N-transformation processes and shaping benthic N isotope dynamics, including that of  $\delta^{15}\text{N-NO}_3^-$ . While  
 643 such process coupling has been examined in the water column (Frey et al., 2014), it remains, to our knowledge, largely  
 644 unexplored in sedimentary environments.

645 To assess the significance of this coupling, we implemented a one-step denitrification approach that bypasses  $\text{NO}_2^-$  as an  
 646 intermediate, replacing the three-step pathway used throughout this paper (Fig. 8). In this simplified model,  $\text{NO}_2^-$  concentrations and isotopic signatures are shaped solely by nitrification (and to a marginal extent, DNRA and anammox), as  
 647 denitrification no longer contributes to  $\text{NO}_2^-$  production. This modification leads to significantly reduced  $\text{NO}_2^-$  accumulation,  
 648 restricted to the upper 0.3 cm, and lower anammox activity, due to a lack of  $\text{NO}_2^-$  substrate below the oxycline. The absence  
 649 of denitrification-derived  $\text{NO}_2^-$  has profound effects on the N isotope dynamics. First, a consistent  $\sim 15\text{\textperthousand}$  offset between  
 650  $\delta^{15}\text{N-NO}_3^-$  and  $\delta^{15}\text{N-NO}_2^-$  is evident across all modelled depths (Fig. 8c). This offset is ascribed to the isotope effect of the  
 651 second nitrification step ( $\varepsilon_{\text{Nitr2}} = -13.7\text{\textperthousand}$ ), and the lack of  $^{15}\text{N}$  enrichment in the  $\text{NO}_2^-$  pool from denitrification. Second, the  
 652 estimated isotope effect for  $\text{NO}_3^-$  reduction ( $\varepsilon_{\text{Den}}$ ) increases to  $5.5 \pm 0.9\text{\textperthousand}$ , nearly double than in the Base scenario, indicating  
 653 that elevated  $\delta^{15}\text{N-NO}_3^-$  values in the field data may, to some extent, reflect  $\text{NO}_2^-$  isotope dynamics, rather than solely the  
 654 effect of  $\text{NO}_3^-$  reduction (Fig. 1).

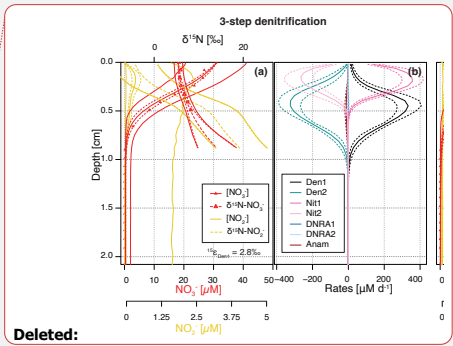


657 These findings emphasise the importance of both  $\text{NO}_2^-$ -producing and -consuming processes in modulating  $\delta^{15}\text{N}-\text{NO}_3^-$ , and  
 658 consequently, estimates of  $\varepsilon_{\text{Den1}}$ . Although nitrification is typically aerobic and denitrification anaerobic, evidence exists that  
 659 indicates spatial overlap of these two processes at the bottom of oxyclines in natural aquatic environments (Frey et al., 2014;  
 660 Granger and Winkel, 2016) at the bottom of the oxycline. In this transition zone,  $\text{NO}_2^-$  produced by either pathway can be  
 661 oxidised to  $\text{NO}_3^-$  or reduced to  $\text{N}_2\text{O}$ ,  $\text{NH}_4^+$  or  $\text{N}_2$  (Fig. 3), significantly affecting its  $\delta^{15}\text{N}$  signature (depending on the N-  
 662 branching). For instance,  $\text{NO}_2^-$  reduction to  $\text{N}_2\text{O}$  enriches the residual  $\text{NO}_2^-$  pool in  $^{15}\text{N}$ . If this  $^{15}\text{N}$ -enriched  $\text{NO}_2^-$  is  
 663 subsequently oxidized to  $\text{NO}_3^-$  (a reaction that exhibits an inverse kinetic isotope effect), the resulting  $\text{NO}_3^-$  will be markedly  
 664 enriched in  $^{15}\text{N}$  (Fig. 1). Such interactions have been shown to influence apparent isotope effects for  $\text{NO}_3^-$  in the water  
 665 column (Frey et al., 2014), and likely exert similar effects in sediments, where sharp redox gradients create overlapping  
 666 zones of nitrification and denitrification. This coupling may explain the discrepancy in estimated  $\varepsilon_{\text{Den1}}$  values between the  
 667 Base scenario ( $2.8 \pm 1.1\%$ ) and the one-step denitrification model approach ( $5.5 \pm 0.9\%$ ).  
 668 Anammox further complicates these dynamics, as it depends on  $\text{NO}_2^-$  excreted into the environment. Without denitrification,  
 669 which releases  $\text{NO}_2^-$  (Sun et al., 2024), anammox is substrate limited (Fig. 8). Thus, while previous benthic studies estimated  
 670 denitrification isotope effects using one-step denitrification approaches (Lehmann et al., 2007), our findings call for the  
 671 adoption of a stepwise modelling approach (Sun et al., 2024) that better captures the interdependence of N-transformation  
 672 pathways, and their integrated effects on  $\text{NO}_3^-$  isotope dynamics. A more detailed examination of these interactions is  
 673 essential for refining our understanding and quantification of isotope effects associated with  $\text{NO}_3^-$  reduction in sedimentary  
 674 systems.



675

676 **Figure 8.** Depth profiles of  $\text{NO}_3^-$  and  $\text{NO}_2^-$  concentrations and N isotopic composition (A,C), and rates of  $\text{NO}_2^-$ -producing and -  
 677 consuming processes (B,D), as simulated by the Base scenario (A,B), and the one-step denitrification approach (C,D). In the one-  
 678 step approach,  $\text{NO}_3^-$  is reduced directly to  $\text{N}_2$ , omitting  $\text{NO}_2^-$  as an intermediate; thus, no  $\text{NO}_2^-$  is produced or consumed through  
 679 denitrification. Dashed lines enclose 95% credibility intervals resulting from parametric uncertainty.



## 681 4.5 Model applicability in distinct scenarios

682 Beyond applying and testing the developed diagenetic N isotope model at our site of interest (Lake Lucerne), we believe its  
683 strength hinges on its versatility to address distinct research questions and objectives. We explored two scenarios as  
684 examples of how the model can be adapted to provide insights into the N cycle in benthic environments and the N isotopic  
685 fingerprints that the combined N-cycling processes leave behind (Fig. 9). Understanding these fingerprints and how they  
686 might be modulated in natural environments (e.g., through the variable balance between individual processes constrained by  
687 environmental conditions) is important for correctly interpreting the distribution of  $^{15}\text{N}/^{14}\text{N}$  ratios in N species as  
688 biogeochemical tracer, helping to pinpoint and disentangle individual N-turnover processes where they co-occur.

689 For comparison purposes, we used the estimated parameters from the Base scenario and modified the relative importance of  
690  $\text{NO}_3^-$  or  $\text{NO}_2^-$  reduction via (i) denitrification vs. DNRA, and (ii) denitrification vs. anammox. This was done by  
691 progressively increasing the factors that define the contributions of DNRA ( $f_{DNRA1,Den1}$  and  $f_{DNRA2,Den2}$ ) and anammox  
692 ( $f_{Anam,Den2}$ ) from 0 (i.e., no DNRA/anammox) to 2 (corresponding to DNRA and anammox accounting for 2/3 of the total  
693  $\text{NO}_3^-$  and  $\text{NO}_2^-$  reduction, respectively). Simultaneously, the rates of the first two steps of denitrification ( $k_{Den1}$  and  $k_{Den2,Den1}$ )  
694 were adjusted to maintain consistent overall  $\text{NO}_3^-$  and  $\text{NO}_2^-$  reduction rates across scenarios. These model results were not  
695 validated against observational data and should therefore be considered as illustrative examples of the model's sensitivity to  
696 selected parameters, rather than as predictions with direct environmental relevance.

697 i. N removal versus N retention

698 The model results confirm the spatial co-occurrence of DNRA and denitrification, with peak  $\text{NO}_3^-$  (data not shown)  
699 and  $\text{NO}_2^-$  (Fig. 9a) reduction activities localized between 0.4-0.6 cm depth. In contrast,  $\text{NH}_4^+$  and  $\text{N}_2$  production  
700 exhibit subtle differences in depth distribution:  $\text{NH}_4^+$  production via DNRA extends across a broader sediment layer  
701 than  $\text{N}_2$  production via denitrification (Fig. 9b). This pattern likely reflects the inhibitory effect of  $\text{O}_2$  on  $\text{N}_2\text{O}$   
702 reduction, the final denitrification step, pushing  $\text{N}_2$  production to deeper, anoxic layers below the oxycline.

703 Reduction of  $\text{NO}_3^-$  exhibits distinct isotope effects depending on the pathway: denitrification ( $\varepsilon_{Den1} \approx 2.8 \pm 1.1\text{\textperthousand}$ )  
704 and DNRA ( $\varepsilon_{DNRA1} \approx 20.0 \pm 2.9\text{\textperthousand}$ ), according to our model estimates (Fig. 5m,v). This large difference reflects the  
705 difficulty of constraining DNRA isotope effects through Bayesian inference, due to its low environmental relevance  
706 in the top 1 cm of Lake Lucerne sediments. Although not proven so far, this isotope offset implies that  $\text{NO}_3^-$   
707 reducers impart distinct isotopic fractionation depending on the pathway, which is rather implausible. However, if  
708 true, increasing DNRA activity would lead to a stronger  $^{15}\text{N}$  enrichment in the residual  $\text{NO}_3^-$  pool (Fig. S6d), with  
709 downstream impacts on the product pools ( $\text{N}_2$  and  $\text{NH}_4^+$ ) (Fig. 9c-d).

710 Denitrification-derived  $\text{N}_2$  mixes with a large ambient  $\text{N}_2$  pool (717  $\mu\text{M}$ ;  $\delta^{15}\text{N} \sim 0\text{\textperthousand}$ ), resulting in slightly elevated  
711  $\delta^{15}\text{N-N}_2$  values in the top 1 cm. While this increase is subtle ( $\Delta\delta^{15}\text{N} < 0.1\text{\textperthousand}$ ), it becomes more pronounced as a  
712 larger fraction of  $\text{NO}_3^-$  (and subsequently  $\text{NO}_2^-$ ) is reduced to  $\text{N}_2$  (denitrification) rather than to  $\text{NH}_4^+$  (DNRA) (Fig.  
713 9c) due to the distinct isotope effects associated with  $\text{NO}_3^-$  reduction via denitrification and DNRA. Under full

714 expression of the denitrification isotope effect (i.e.,  $\varepsilon_{Denl} \approx 20\text{\textperthousand}$ ),  $\delta^{15}\text{N-N}_2$  much lower than 0‰ would be expected;  
715 in contrast,  $\varepsilon_{Denl} \approx 2.8\text{\textperthousand}$  likely suppresses such isotopic dynamics, resulting in only subtle  $\delta^{15}\text{N-N}_2$  changes. As  
716 more  $\text{NO}_3^-$  is reduced via DNRA ( $\varepsilon_{DNRAI} \approx 20.0\%$ ) than via denitrification ( $\varepsilon_{Denl} \approx 2.8\text{\textperthousand}$ ), a stronger  $^{15}\text{N}$  depletion  
717 is expected in the  $\text{NO}_2^-$  pool; if this  $\text{NO}_2^-$  is then reduced to  $\text{N}_2$  will lead to lower  $\delta^{15}\text{N-N}_2$  than in a purely-  
718 denitrifying case. Such interaction can explain the shift toward lower  $\delta^{15}\text{N-N}_2$  values as  $\text{NO}_3^-$  is increasingly  
719 reduced via DNRA with a strong isotope effect recorded in our model. Thus, the slightly elevated  $\delta^{15}\text{N-N}_2$  values  
720 observed in our model confirms that denitrification dominates over DNRA, and operates with a reduced isotope  
721 effect (2.8‰), likely due to diffusive limitation.

722 In contrast, enhanced DNRA activity leads to  $\text{NH}_4^+$  accumulation and a progressive decrease in  $\delta^{15}\text{N-NH}_4^+$  in the  
723 upper 0.5 cm, consistent with strong isotopic fractionation during DNRA (Fig. 9d). This  $\text{NH}_4^+$  pool appears to  
724 promote nitrification, as indicated by higher  $\text{NH}_4^+$  and  $\text{NO}_2^-$  oxidation rates (Fig. S6a-b), resulting in the production  
725 of  $^{15}\text{N}$ -depleted  $\text{NO}_2^-$  (Fig. S6c). Notably, if this isotopically light  $\text{NO}_2^-$  is subsequently reduced via denitrification,  
726 it can lead to the formation of  $\text{N}_2$  with unusually low  $\delta^{15}\text{N}$  values, even if denitrification itself operates with a  
727 modest isotope effect. This secondary effect underscores how DNRA not only alters substrate availability but also  
728 indirectly influences the isotopic composition of denitrification end products. The strong spatial overlap of DNRA,  
729 denitrification and nitrification highlights the central role of DNRA in fuelling internal N recycling (Wang et al.,  
730 2020) with implications that extend to the  $\delta^{15}\text{N}$  of both intermediate and terminal N pools.

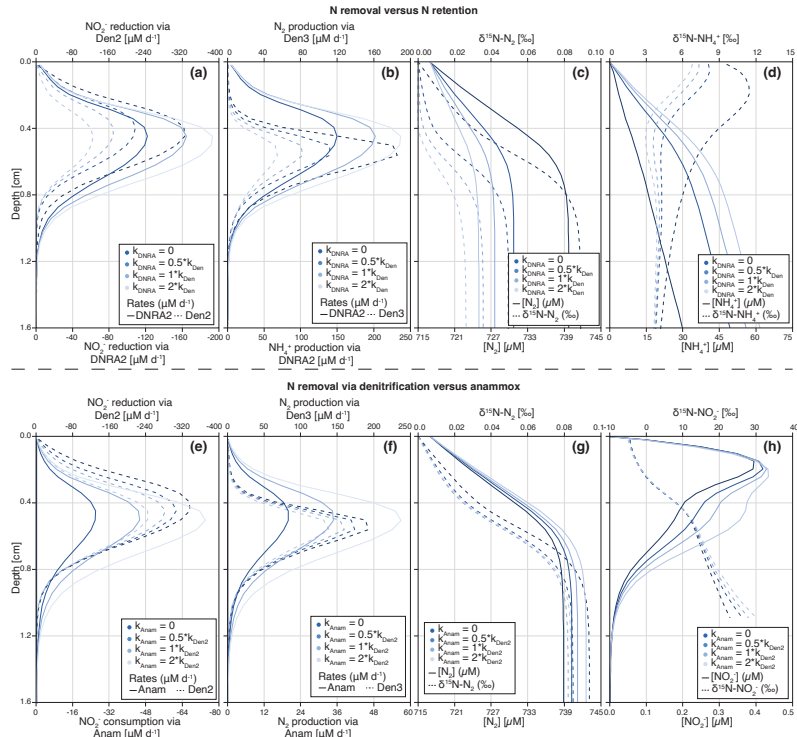
731 Thus, if  $\text{NO}_3^-$  reduction via DNRA and denitrification occurs with distinct isotope effects, our model has the  
732 potential to disentangle their respective contributions based on  $\delta^{15}\text{N}$  profiles of  $\text{NO}_3^-$  and  $\text{NH}_4^+$ , and to a lesser  
733 extent of  $\text{N}_2$  and  $\text{NO}_2^-$ . Importantly, our results underscore a potentially critical, yet underappreciated, coupling  
734 between DNRA and nitrification in benthic environments. If verified, this interaction, largely invisible in  
735 concentration profiles alone, can significantly influence isotopic signatures and must be considered when  
736 interpreting sediment N dynamics through an isotope lens.

737 ii. N removal via denitrification versus anammox

738 The results for this case scenario reveal, somewhat unexpectedly, some similarities between denitrification and  
739 anammox with respect to  $\text{NO}_2^-$  reduction to  $\text{N}_2$  and associated N isotope signatures. The isotope effects associated  
740 with denitrification are low (2.8‰ for  $\text{NO}_3^-$  reduction and 7.9‰ for  $\text{NO}_2^-$  reduction), whereas anammox imparts  
741 stronger isotopic fractionation (14.4‰ for  $\text{NO}_2^-$  reduction to  $\text{N}_2$  and -30.0‰ for its oxidation to  $\text{NO}_3^-$ ). These values  
742 reflect parameter estimations specific to Lake Lucerne's surface sediments (upper 1 cm), where anammox activity  
743 is low.

744 Both  $\text{NO}_2^-$  reduction and  $\text{N}_2$  production peak around 0.5 cm depth, with minor differences in the thickness of the  
745 active layer due to variations in substrate affinity between modelled processes (Fig. 9e-f). The total rate of  $\text{NO}_2^-$   
746 reduction to  $\text{N}_2$ , via either anammox or denitrification, remains consistent across all case scenarios. Nonetheless,

747 slight differences can be observed in some N pools as anammox becomes the dominant fixed-N loss path. Increased  
748 anammox activity leads to elevated  $\text{N}_2$  and  $\text{NO}_2^-$  concentrations (Fig. 9g-h), likely due to the use of  $\text{NH}_4^+$  as a  
749 substrate, which mitigates substrate limitation under low  $\text{NO}_2^-$  availability (i.e., 1.3 mol  $\text{NO}_2^-$  needed to produce 1  
750 mol  $\text{N}_2$  via anammox versus 2 mol  $\text{NO}_2^-$  via denitrification). When anammox prevails,  $\delta^{15}\text{N-NO}_2^-$  values increase  
751 due to the stronger isotope effect associated with  $\text{NO}_2^-$  reduction via anammox relative to denitrification. This  
752 enrichment is partially counterbalanced by the inverse kinetic isotope effect during  $\text{NO}_2^-$  oxidation to  $\text{NO}_3^-$  (Brunner  
753 et al., 2013), leading to  $^{15}\text{N}$ -enriched  $\text{NO}_3^-$  below 0.8 cm; notably, this isotopic shift occurs without significant  
754 changes in total  $\text{NO}_3^-$  concentrations (Fig. S6g-h). Lastly, substantial differences emerge in the  $\text{NH}_4^+$  pool: higher  
755 anammox activity correlates with lower  $\text{NH}_4^+$  concentrations and elevated  $\delta^{15}\text{N-NH}_4^+$  values throughout most of the  
756 sampled depths (Fig. S6e-f). This isotopic enrichment likely overlaps with the effect of nitrification on the  $\text{NH}_4^+$   
757 pool in the upper 0.3 cm.  
758 While some differentiation between denitrification and anammox is evident in the isotope signatures of  $\text{NO}_3^-$  and  
759  $\text{NH}_4^+$ , the expected contrasts in the  $\text{NO}_2^-$  and  $\text{N}_2$  pools are surprisingly muted. This near-indistinguishability in  
760 isotopic outcomes suggests a degree of functional and isotopic redundancy between the two pathways under the  
761 modelled conditions. These results highlight the need for further investigation, particularly through refined isotope-  
762 based methods (e.g., inclusion of  $\text{NO}_x$  O-isotopes or clumped nitrate isotopes) and more mechanistic modelling, to  
763 distinguish the respective contributions of denitrification and anammox to N removal in sedimentary systems.



764

765 **Figure 9.** Depth profiles of process rates, solute concentrations and  $\delta^{15}\text{N}$  values for the two idealized case scenarios investigated: (i)  
766  $\text{NO}_2^-$  reduction via DNRA and denitrification (a-d), (ii)  $\text{N}_2$  production via anammox and denitrification (e-h). Shadings represent  
767 different model scenarios within each case, as defined in the legend. For case (i), colour shading lightens with increasing  
768 contribution of DNRA (relative to denitrification) to total  $\text{NO}_2^-$  reduction. DNRA accounts for 0% ( $f_{\text{DNRA}} = 0$ ), 33% ( $f_{\text{DNRA}} = 0.5$ ),  
769 50% ( $f_{\text{DNRA}} = 1$ ) and 66% ( $f_{\text{DNRA}} = 2$ ) of total  $\text{NO}_2^-$  reduction (panel a). The resulting effects on the production rates of  $\text{NH}_4^+$  and  $\text{N}_2$   
770 (b), as well as on their concentrations and N isotopic composition (c-d), are shown. For case (ii), colour shading lightens with  
771 increasing contribution of anammox (relative to denitrification) to total  $\text{NO}_2^-$  consumption and associated  $\text{N}_2$  production.  
772 Anammox contributes 0% ( $f_{\text{Anam}} = 0$ ), 33% ( $f_{\text{Anam}} = 0.5$ ), 50% ( $f_{\text{Anam}} = 1$ ) and 66% ( $f_{\text{Anam}} = 2$ ) of total  $\text{NO}_2^-$  consumption (e-f). The  
773 resulting impacts on  $\text{N}_2$  and  $\text{NO}_2^-$  concentrations and  $\delta^{15}\text{N}$  values are shown in panels g-h.

## 774 5. Conclusions

775 We developed a comprehensive diagenetic N isotope model that integrates multiple N transformations in benthic  
776 environments. The model's complexity requires the use of prior knowledge in addition to the observed data, in order to  
777 achieve the most plausible descriptions of the ongoing processes. To address uncertainty in prior knowledge, and to reduce

778 structural errors associated with fixed parameter values, we applied Bayesian inference for a large parameter set (~60) for  
779 data analysis. The computational demands of this approach were met by implementing the model in Julia, with compatibility  
780 for automatic differentiation to allow for advanced Markov chain Monte Carlo algorithms needed for Bayesian inference.  
781 Despite these optimization efforts to enhance efficiency, inference runs still took 2-3 weeks of computation time (in addition  
782 to preceding simulations to reduce burn-in) to achieve sufficiently good convergence of the Markov chains of the posterior  
783 parameter distribution. Alongside concentrations and  $\delta^{15}\text{N}$  values for different N species, the model provides depth profiles  
784 of process rates and all fluxes, including their uncertainties. These outputs enable a detailed assessment of the processes  
785 shaping N cycling (i.e., concentration profiles) and isotope patterns in sediments.

786 Application of the developed model to a test dataset from Lake Lucerne successfully reproduced measured profiles of  $\text{O}_2$ ,  
787  $\text{SO}_4^{2-}$ ,  $\text{NH}_4^+$ ,  $\text{NO}_2^-$ ,  $\text{NO}_3^-$ ,  $\delta^{15}\text{N}-\text{NH}_4^+$ , and  $\delta^{15}\text{N}-\text{NO}_3^-$ . The model also produced realistic vertical distributions of conversion  
788 rates, revealing clear depth-dependent zonation. Most marginal posterior distributions of estimated parameters were in good  
789 agreement with their priors. Yet, strong deviations were observed for the N isotope effect associated with the first step of  
790 denitrification,  $\varepsilon_{\text{Den1}}$ , which was estimated at  $\sim 2.8 \pm 1.1\text{‰}$ , significantly lower than the expected  $\sim 20\text{‰}$ . These findings were  
791 confirmed by additional simulations performed using narrower priors and a fixed  $\varepsilon_{\text{Den1}}$  value of  $20\text{‰}$ , both of which resulted  
792 in a substantial deterioration in the model's ability to reproduce  $\delta^{15}\text{N}-\text{NO}_3^-$  profiles. This, in turn, can be taken as indication  
793 for a suppressed denitrification  $\text{NO}_3^-$  isotope effect at the porewater level in Lake Lucerne, potentially due to process  
794 coupling via  $\text{NO}_2^-$ . The model's ability to quantify such interactions, which can be difficult to discern in situ or from field  
795 data alone, is a key strength of this stepwise model framework. [A manuscript assessing such dynamics across distinct sites is](#)  
796 [currently being prepared to further corroborate these findings.](#)

797 Further sensitivity tests highlighted that the model could still achieve good fits to the observational data even when certain  
798 individual processes were excluded, demonstrating the critical role of prior knowledge regarding estimated parameters and  
799 their associated uncertainties.

800 Overall, this study presents [one of](#) the first comprehensive diagenetic N isotope models that explicitly incorporate multiple N  
801 transformation pathways in a stepwise manner [and are](#) validated against field measurements. Rather than serving as a purely  
802 predictive tool, this model is intended to stimulate scientific discussion on the quantification of N transformations and  
803 isotope dynamics in sediments based on observed data. Future developments could focus on improving identifiability  
804 through additional, targeted observations, expanding model validation across distinct benthic environments, and the  
805 incorporating additional isotope tracers, such as  $\delta^{18}\text{O}$  of  $\text{NO}_3^-$  and  $\text{NO}_2^-$ , to further strengthen the model structure and  
806 improve its reliability.

**Deleted:** s

**Deleted:** ,

Table A1. Overview of all modelled N-transformation pathways, including their stoichiometry and governing equations.  $R$  denotes the  $^{15}\text{N}/[^{14}\text{N}+^{15}\text{N}]$  ratio derived from OM. The  $\gamma$  parameter defines the fraction of  $\text{NH}_4^+$  released during OM mineralization for each reaction. Anammox encompasses both the comproportionation of  $\text{NH}_4^+$  and  $\text{NO}_2^-$  to  $\text{N}_2$ , defined as the main ("m") reaction, and the production of  $\text{NO}_3^-$  from  $\text{NO}_2^-$ , defined as the side ("s") reaction.

Process	Step	$^{14}\text{N}$	$\text{NH}_4^+$	$^{15}\text{N}$	$\text{NO}_2^-$	$^{14}\text{N}$	$^{15}\text{N}$	$\text{NO}_3^-$	$^{14}\text{N}$	$^{15}\text{N}$	$\text{NO}_2$	$^{14}\text{N}$	$^{15}\text{N}$	$\text{N}_2$	$^{14}\text{N}$	$^{15}\text{N}$	$\text{O}_2$	$\text{SO}_4^{2-}$	Rate
Oxic min.		$\gamma_{\text{MinOx}}$	$(1-R)$	$\gamma_{\text{MinOx}}, R$															$r^*_{\text{MinOx}}$
Denitrification	[1]	$\gamma_{\text{Den1}} (1-R)$	$\gamma_{\text{Den1}} R$	1	-1														$r^*_{\text{Den1}} [^{14}\text{NO}_3^-]$
	[2]	$\gamma_{\text{Den1}} (1-R)$	$\gamma_{\text{Den1}} R$	1	-1	1													$r^*_{\text{Den1}} [^{15}\text{NO}_3^-] (1-\mathcal{E}_{\text{Den1}})$
		$2\gamma_{\text{Den2}} (1-R)$	$2\gamma_{\text{Den2}} R$	-2															$r^*_{\text{Den2}} [^{14}\text{NO}_2^-] [^{15}\text{NO}_2^-] (1-\mathcal{E}_{\text{Den2}})$
		$2\gamma_{\text{Den2}} (1-R)$	$2\gamma_{\text{Den2}} R$	-1	-1	1													$2r^*_{\text{Den2}} [^{14}\text{NO}_2^-] [^{15}\text{NO}_2^-] (1-\mathcal{E}_{\text{Den2}})$
		$2\gamma_{\text{Den2}} (1-R)$	$2\gamma_{\text{Den2}} R$	-2															$r^*_{\text{Den2}} [^{15}\text{NO}_2^-] [^{15}\text{NO}_2^-] (1-\mathcal{E}_{\text{Den2}})^2$
[3]	$\gamma_{\text{Den3}} (1-R)$	$\gamma_{\text{Den3}} R$																	$r^*_{\text{Den3}} [^{14}\text{N}_2\text{O}]$
	$\gamma_{\text{Den3}} (1-R)$	$\gamma_{\text{Den3}} R$																	$r^*_{\text{Den3}} [^{14}\text{N}_2\text{O}] (1-\mathcal{E}_{\text{Den3}})$
	$\gamma_{\text{Den3}} (1-R)$	$\gamma_{\text{Den3}} R$																	$r^*_{\text{Den3}} [^{15}\text{N}_2\text{O}] (1-\mathcal{E}_{\text{Den3}})$
Sulfate reduction		$\gamma_{\text{MinSulfRed}} (1-R)$	$\gamma_{\text{MinSulfRed}} R$																-1
Anaerobic min.		$1-R$	$R$																$r^*_{\text{MinAer}}$
Nitrification	[1]	-1		1															-1.5
		-2		-1	1													$r^*_{\text{Nita}} [^{14}\text{NH}_4^+]$	
		-1		-1														$r^*_{\text{Nita}} [^{15}\text{NH}_4^+] (1-\mathcal{E}_{\text{Nita}, \text{NO}_2})$	
[2]		-2																$r^*_{\text{Nita}} [^{14}\text{NH}_4^+] [^{14}\text{NH}_4^+] (1-\mathcal{E}_{\text{Nita}, \text{NO}_2})$	
		-1																$2r^*_{\text{Nita}} [^{14}\text{NH}_4^+] [^{14}\text{NH}_4^+] (1-\mathcal{E}_{\text{Nita}, \text{NO}_2})$	
		-1																$r^*_{\text{Nita}} [^{15}\text{NH}_4^+] [^{15}\text{NH}_4^+] (1-\mathcal{E}_{\text{Nita}, \text{NO}_2})$	
		-1																$r^*_{\text{Nita}} [^{15}\text{NH}_4^+] [^{15}\text{NH}_4^+] (1-\mathcal{E}_{\text{Nita}, \text{NO}_2})$	
Anammox	[m]	-1		-1															$r^*_{\text{Anam}} [^{14}\text{NH}_4^+] [^{14}\text{NO}_2^-]$
		-1		-1	-1													$r^*_{\text{Anam}} [^{14}\text{NH}_4^+] [^{15}\text{NO}_2^-] (1-\mathcal{E}_{\text{Anam}, \text{NO}_2})$	
		-1		-1	-1													$r^*_{\text{Anam}} [^{15}\text{NH}_4^+] [^{14}\text{NO}_2^-] (1-\mathcal{E}_{\text{Anam}, \text{NH}_4})$	
[s]		-1		-1	1													$r^*_{\text{Anam}} [^{15}\text{NH}_4^+] [^{15}\text{NO}_2^-] (1-\mathcal{E}_{\text{Anam}, \text{NH}_4})$	
		-1		-1	1													$r^*_{\text{Anam}} [^{15}\text{NH}_4^+] [^{15}\text{NO}_2^-] (1-\mathcal{E}_{\text{Anam}, \text{NH}_4})$	
		-1		-1	1													$r^*_{\text{Anam}} [^{15}\text{NH}_4^+] [^{15}\text{NO}_2^-] (1-\mathcal{E}_{\text{Anam}, \text{NH}_4})$	
		-1		-1	1													$r^*_{\text{Anam}} [^{15}\text{NH}_4^+] [^{15}\text{NO}_2^-] (1-\mathcal{E}_{\text{Anam}, \text{NH}_4})$	
		-1		-1	1													$r^*_{\text{Anam}} [^{15}\text{NH}_4^+] [^{15}\text{NO}_2^-] (1-\mathcal{E}_{\text{Anam}, \text{NH}_4})$	
DNRA	[1]	$\gamma_{\text{DNRA1}} (1-R)$	$\gamma_{\text{DNRA1}} R$	1	-1														$r^*_{\text{DNRA1}} [^{14}\text{NO}_3^-]$
		$\gamma_{\text{DNRA1}} (1-R)$	$\gamma_{\text{DNRA1}} R$	1	-1														$r^*_{\text{DNRA1}} [^{15}\text{NO}_3^-] (1-\mathcal{E}_{\text{DNRA1}})$

	[2]	$1 + \gamma_{\text{DNRA2}} (1-R)$	$\gamma_{\text{DNRA2}} R$	-1				$r'_{\text{DNRA2}} [{}^{14}\text{NO}_2]$
		$\gamma_{\text{DNRA2}} (1-R)$	$1 + \gamma_{\text{DNRA2}} R$	-1				$r'_{\text{DNRA2}} [{}^{14}\text{NO}_2] (1 - \varepsilon_{\text{DNRA2}})$
813	$r_{\text{MinOx}}$	$= k_{\text{MinOx}} \frac{[O_2]}{K_{O_2,\text{MinOx}} + [O_2]}$		$r_{\text{MinAnae}} = k_{\text{MinAnae}} \frac{K_{\text{NO3,MinAnae}}}{K_{\text{NO3,MinAnae}} + [{}^{14}\text{NO}_3] + [{}^{15}\text{NO}_3]} \frac{K_{O_2,\text{MinAnae}}}{K_{O_2,\text{MinAnae}} + [O_2]}$				
814	$r'_{\text{MinSulfRed}}$	$= k_{\text{MinSulfRed}} \frac{[O_2]}{K_{\text{SO}_4,\text{MinSulfRed}} + [O_2]}$	$\frac{[SO_4^{2-}]}{K_{\text{SO}_4,\text{MinSulfRed}} + [SO_4^{2-}]} \frac{K_{\text{NO3,MinSulfRed}}}{K_{\text{NO3,MinSulfRed}} + [NO_3^-]} \frac{K_{O_2,\text{MinSulfRed}}}{K_{O_2,\text{MinSulfRed}} + [O_2]}$					
815	$r'_{\text{Anam}}$	$= k_{\text{Anam}} \frac{1}{K_{\text{NH}_4,\text{Anam}} + [{}^{14}\text{NH}_4^+] + [{}^{15}\text{NH}_4^+] + K_{\text{NO2,Anam}} + [{}^{14}\text{NO}_2] + [{}^{15}\text{NO}_2]} \frac{K_{O_2,\text{Anam}}}{K_{O_2,\text{Anam}} + [O_2]}$						
816	$r'_{\text{Nit1a}}$	$= k_{\text{Nit1}} (1 - f_{\text{N2O,Nit1}}) \frac{1}{K_{\text{NH}_4,\text{Nit1}} + [{}^{14}\text{NH}_4^+] + [{}^{15}\text{NH}_4^+] + K_{\text{O2,Nit1}} + [O_2]} \frac{[O_2]}{r'_{\text{Nit1b}} = k_{\text{Nit1}} f_{\text{N2O,Nit1}} \frac{1}{(K_{\text{NH}_4,\text{Nit1}} + [{}^{14}\text{NH}_4^+] + [{}^{15}\text{NH}_4^+] + K_{\text{O2,Nit1}} + [O_2])^2} \frac{[O_2]}{K_{\text{O2,Nit1}} + [O_2]}}$						
817	$r'_{\text{Nit2}}$	$= k_{\text{Nit2}} \frac{1}{K_{\text{NO2,Nit2}} + [{}^{14}\text{NO}_2] + [{}^{15}\text{NO}_2]} \frac{[O_2]}{K_{\text{O2,Nit2}} + [O_2]}$						
818	$r'_{\text{Den1}}$	$= k_{\text{Den1}} \frac{1}{K_{\text{NO2,Den1}} + [{}^{14}\text{NO}_3] + [{}^{15}\text{NO}_3]} \frac{K_{O2,Den1}}{K_{O2,Den1} + [O_2]} \frac{r'_{\text{Den2}} = k_{\text{Den2}} \frac{1}{(K_{\text{NO2,Den2}} + [{}^{14}\text{NO}_2] + [{}^{15}\text{NO}_2])^2} \frac{K_{O2,Den2}}{K_{O2,Den2} + [O_2]}}$						
819	$r'_{\text{Den3}}$	$= k_{\text{Den3}} \frac{1}{K_{\text{NO2,Den3}} + [{}^{14}\text{NO}_3] + [{}^{15}\text{NO}_3]} \frac{K_{O2,Den3}}{K_{O2,Den3} + [O_2]} \frac{r'_{\text{DNRA2}} = k_{\text{DNRA2}} \frac{1}{K_{\text{NO2,DNRA2}} + [{}^{14}\text{NO}_2] + [{}^{15}\text{NO}_2]} \frac{K_{O2,DNRA2}}{K_{O2,DNRA2} + [O_2]}}$						
820	$r'_{\text{DNRA1}}$	$= k_{\text{DNRA1}} \frac{1}{K_{\text{NO3,DNRA1}} + [{}^{14}\text{NO}_3] + [{}^{15}\text{NO}_3]} \frac{K_{O2,DNRA1}}{K_{O2,DNRA1} + [O_2]} \frac{r'_{\text{DNRA2}} = k_{\text{DNRA2}} \frac{1}{K_{\text{NO2,DNRA2}} + [{}^{14}\text{NO}_2] + [{}^{15}\text{NO}_2]} \frac{K_{O2,DNRA2}}{K_{O2,DNRA2} + [O_2]}}$						
821	$f_{\text{N2O,Nit1}}$	$= b_{\text{N2O,Nit1}} \frac{a_{\text{N2O,Nit1}}}{a_{\text{N2O,Nit1}} + [O_2]}$						
822	$k_{\text{Den2}}$	$= f_{\text{Den2,Den1}} k_{\text{Den1}}$	$k_{\text{Den3}} = f_{\text{Den3,Den1}} k_{\text{Den1}}$		$k_{\text{Nit2}} = f_{\text{Nit2,Nit1}} k_{\text{Nit1}}$			
823	$k_{\text{Anam}}$	$= f_{\text{Anam,Den2}} k_{\text{Den2}}$	$k_{\text{DNRA1}} = f_{\text{DNRA1,Den1}} k_{\text{Den1}}$		$k_{\text{DNRA2}} = f_{\text{DNRA2,Den2}} k_{\text{Den2}}$			

824 **Appendix B: Reaction-diffusion model**825 Nomenclature

826	$t$	time [d]
827	$z$	depth coordinate within sediment (0 at the sediment surface, $d$ at the lower boundary of the modelled sediment layer) [cm]
828	$d$	depth of the modelled sediment layer [cm]
829	$C(z,t)$	substance concentration (mass per volume of water) as a function of depth and time
830	$p(z)$	porosity of the sediment (water volume divided by sediment volume) as a function of sediment depth
831	$D(z)$	diffusivity of the substance in the water as a function of depth (usually constant and equal to the molecular diffusion coefficient; however, bioturbation could be modelled as an increase in diffusivity close to the sediment surface)
832	$r(C)$	transformation rate of the substance (mass per volume of water per unit of time)
833	$C_0$	substance concentration at the sediment surface
834	$F_d$	substance flux from deep sediment into the modelled sediment layer at the lower boundary of the modelled sediment layer (mass per unit of total sediment surface and per unit of time)

835 Partial Differential Equation for Sediment Layer

836 Mass balance within the sediment layer:

837 
$$p \frac{\partial C}{\partial t} - \frac{\partial}{\partial z} \left( D p \frac{\partial C}{\partial z} \right) = p r$$

838 Differential equation for concentration:

839 
$$\frac{\partial C}{\partial t} = \frac{1}{p} \frac{\partial}{\partial z} \left( D p \frac{\partial C}{\partial z} \right) + r$$

840 Diffusion (molecular diffusion corrected for tortuosity, and bioturbation):

841 
$$D = \frac{D_{\text{mol}}}{a_{\text{tort}} p^{1-m_{\text{tort}}}} + D_{\text{bio}} e^{-\frac{z}{d_{\text{bio}}}}$$

842 Boundary conditions:

843 
$$C(0, t) = C_0, \quad D(d, t)p(d, t) \frac{\partial C}{\partial z}(d, t) = F_d$$

844

845 For N compounds with a single N atom, the boundary conditions are calculated from total concentrations,  $C_{\text{tot}}$ , and  $\delta^{15}\text{N}$  as follows:

846 
$$r = \left( \frac{\delta^{15}\text{N}}{1000} + 1 \right) R_{\text{std}} \quad C_{^{14}\text{N}} = \frac{1}{1+r} C_{\text{tot}} \quad C_{^{15}\text{N}} = \frac{r}{1+r} C_{\text{tot}}$$

847 For N compounds with two N atoms, the boundary conditions are calculated from total concentrations,  $C_{\text{tot}}$ , and  $\delta^{15}\text{N}$  as follows (Drury et al., 1987):

848 
$$r = \left( \frac{\delta^{15}\text{N}}{1000} + 1 \right) R_{\text{std}} \quad C_{^{14}\text{N}^{14}\text{N}} = \frac{1}{1+2r+r^2} C_{\text{tot}} \quad C_{^{15}\text{N}^{14}\text{N}} = \frac{2r}{1+2r+r^2} C_{\text{tot}} \quad C_{^{15}\text{N}^{15}\text{N}} = \frac{r^2}{1+2r+r^2} C_{\text{tot}}$$

155 **Appendix C: Prior values for inference**

156 Table C1. Model parameters estimated using Bayesian inference, alongside their prior values and associated uncertainties. The posterior values (estimated mean with their standard deviation  
157 for the base scenario (Section 4.1) are also reported. Parameters are grouped into three categories: (A) reaction rates parameters (i.e., defining process kinetics), (B) isotope parameters (i.e.,  
158 isotope effects for the modelled processes and the N isotopic composition of OM), and (C) parameters used in the one-step denitrification approach ( $\text{NO}_3^- \rightarrow \text{N}_2$  instead of  $\text{NO}_3^- \rightarrow \text{NO}_2^- \rightarrow \text{N}_2$ ). Where a wide range of values was reported in the literature, the most relevant value for benthic environments was selected, and the corresponding reference is reported.

Description	Symbol	Distribution	Mean	St.deviation	Reference(s)	Posterior mean ( $\pm \text{SD}$ )
<i>(A) Reaction rate parameters</i>						
<u>Aerobic mineralization</u>	$k_{MnO_2}$	Uniform	—	—	—	<u><math>3330 (\pm 220) \mu\text{M d}^{-1}</math></u>
	$K_{O2,MnO_2}$	Lognormal	$8 \mu\text{M}$	20%	(Rooze and Meile, 2016)	<u><math>6.9 (\pm 0.9) \mu\text{M}</math></u>
	$\gamma_{NH4,MnO_2}$	Lognormal	0.1509	10%	Stoichiometry	<u><math>0.15 (\pm 0.01)</math></u>
<u>Anaerobic mineralization</u>	$k_{Mn,tnue}$	Uniform	—	—	—	<u><math>0.13 (\pm 0.03) \mu\text{M d}^{-1}</math></u>
	$K_{O2,Mn,tnue}$	Lognormal	$5 \mu\text{M}$	20%	(Paraska et al., 2011)	<u><math>5.1 (\pm 0.7) \mu\text{M}</math></u>
	$K_{NO3,Mn,tnue}$	Lognormal	$5 \mu\text{M}$	20%	(Paraska et al., 2011)	<u><math>4.9 (\pm 0.7) \mu\text{M}</math></u>
<u>Sulfate reduction counted to mineralization</u>	$k_{MnSulfRed}$	Uniform	—	—	—	<u><math>41 (\pm 1) \mu\text{M d}^{-1}</math></u>
	$K_{O2,MnSulfRed}$	Lognormal	$5 \mu\text{M}$	20%	Assumed to be comparable to $K_{O2,Mn,tnue}$	<u><math>5.1 (\pm 0.7) \mu\text{M}</math></u>
	$K_{NO3,MnSulfRed}$	Lognormal	$5 \mu\text{M}$	20%	Assumed to be comparable to $K_{NO3,Mn,tnue}$	<u><math>5.4 (\pm 0.7) \mu\text{M}</math></u>
	$K_{SO4,MnSulfRed}$	Lognormal	$20 \mu\text{M}$	20%	(Richards and Pallud, 2016)	<u><math>44 (\pm 1) \mu\text{M}</math></u>
	$\gamma_{NH4,MnSulfRed}$	Lognormal	0.3019	10%	Stoichiometry	<u><math>0.26 (\pm 0.02)</math></u>
<u>Nitrification</u>	$k_{N2I}$	Uniform	—	—	—	<u><math>680 (\pm 79) \mu\text{M d}^{-1}</math></u>
	$K_{O2,N2I}$	Lognormal	$3.5 \mu\text{M}$	20%	(Martin et al., 2019)	<u><math>3.1 (\pm 0.4) \mu\text{M}</math></u>
	$K_{NH4,N2I}$	Lognormal	$2.0 \mu\text{M}$	20%	(Wyffels et al., 2004)	<u><math>2.2 (\pm 0.3) \mu\text{M}</math></u>
	$a$	Lognormal	$0.2 \mu\text{M}$	10%	(Ji et al., 2018)	<u><math>0.20 (\pm 0.02) \mu\text{M}</math></u>
	$b$	Lognormal	0.08	10%	(Ji et al., 2018)	<u><math>0.080 (\pm 0.006)</math></u>
[2]	$f_{N2I2}$	Lognormal	1	50%	—	<u><math>1.2 (\pm 0.2)</math></u>
	$K_{O2,N2I2}$	Lognormal	$0.8 \mu\text{M}$	20%	(Martin et al., 2019)	<u><math>0.8 (\pm 0.1) \mu\text{M}</math></u>
	$K_{NO2,N2I2}$	Lognormal	$0.8 \mu\text{M}$	20%	(Wyffels et al., 2004)	<u><math>0.7 (\pm 0.1) \mu\text{M}</math></u>
<u>Denitrification</u>	$k_{Den}$	Uniform	—	—	—	<u><math>462 (\pm 57) \mu\text{M d}^{-1}</math></u>
	$K_{O2,Den}$	Lognormal	$3 \mu\text{M}$	20%	(Wenk et al., 2014)	<u><math>2.9 (\pm 0.4) \mu\text{M}</math></u>
	$K_{NO3,Den}$	Lognormal	$2.46 \mu\text{M}$	20%	(Su et al., 2023)	<u><math>2.3 (\pm 0.3) \mu\text{M}</math></u>

		Fraction of $\text{NH}_4^+$ produced	$\gamma_{\text{NH}_4, \text{Den}l}$	Lognormal	0.0755	10%	Stoichiometry	
[2]	Reaction rate factor	$f_{\text{Den}2}$	Lognormal	3	50%		<u>3.4 (± 0.6)</u>	
	$\text{O}_2$ inhibition constant	$K_{\text{O}_2, \text{Den}2}$	Lognormal	3 $\mu\text{M}$	20%	Assumed to be comparable to $K_{\text{O}_2, \text{Den}l}$	<u>2.9 (± 0.4) <math>\mu\text{M}</math></u>	
	$\text{NO}_3^-$ limitation constant	$K_{\text{NO}_3, \text{Den}2}$	Lognormal	0.41 $\mu\text{M}$	20%	(Su et al., 2023)	<u>0.37 (± 0.05) <math>\mu\text{M}</math></u>	
	Fraction of $\text{NH}_4^+$ produced	$\gamma_{\text{NH}_4, \text{Den}2}$	Lognormal	0.0755	10%	Stoichiometry	<u>0.073 (± 0.006)</u>	
[3]	Reaction rate factor	$f_{\text{Den}3}$	Lognormal	3	50%		<u>2.3 (± 0.4)</u>	
	$\text{O}_2$ inhibition constant	$K_{\text{O}_2, \text{Den}3}$	Lognormal	0.1 $\mu\text{M}$	20%	(Suenaga et al., 2018)	<u>0.10 (± 0.01) <math>\mu\text{M}</math></u>	
	$\text{N}_2\text{O}$ limitation constant	$K_{\text{N}_2\text{O}, \text{Den}3}$	Lognormal	3.7 $\mu\text{M}$	20%	(Suenaga et al., 2018)	<u>3.6 (± 0.5) <math>\mu\text{M}</math></u>	
	Fraction of $\text{NH}_4^+$ produced	$\gamma_{\text{NH}_4, \text{Den}3}$	Lognormal	0.0755	10%	Stoichiometry	<u>0.074 (± 0.006)</u>	
DNRA	Reaction rate factor	$f_{\text{DNRA}, \text{I}, \text{Den}l}$	Lognormal	0.005	25%	$^{15}\text{N}$ -tracer incubations (this study)	<u>0.0049 (± 0.0008)</u>	
	$\text{O}_2$ inhibition constant	$K_{\text{O}_2, \text{DNRA}l}$	Lognormal	3 $\mu\text{M}$	20%	Assumed to be comparable to $K_{\text{O}_2, \text{Den}l}$	<u>2.9 (± 0.4) <math>\mu\text{M}</math></u>	
	$\text{NO}_3^-$ limitation constant	$K_{\text{NO}_3, \text{DNRA}l}$	Lognormal	2.46 $\mu\text{M}$	20%	Assumed to be comparable to $K_{\text{NO}_3, \text{Den}l}$	<u>2.5 (± 0.3) <math>\mu\text{M}</math></u>	
	Fraction of $\text{NH}_4^+$ produced	$\gamma_{\text{NH}_4, \text{DNRA}l}$	Lognormal	0.0755	10%	Stoichiometry	<u>0.076 (± 0.006)</u>	
[2]	Reaction rate factor	$f_{\text{DNRA}, \text{I}, \text{Den}2}$	Lognormal	0.005	25%	$^{15}\text{N}$ -tracer incubations (this study)	<u>0.0047 (± 0.0008)</u>	
	$\text{O}_2$ inhibition constant	$K_{\text{O}_2, \text{DNRA}2}$	Lognormal	3 $\mu\text{M}$	20%	Assumed to be comparable to $K_{\text{O}_2, \text{Den}2}$	<u>3.1 (± 0.4) <math>\mu\text{M}</math></u>	
	$\text{NO}_3^-$ limitation constant	$K_{\text{NO}_3, \text{DNRA}2}$	Lognormal	0.41 $\mu\text{M}$	20%	Assumed to be comparable to $K_{\text{NO}_3, \text{Den}2}$	<u>0.43 (± 0.06) <math>\mu\text{M}</math></u>	
	Fraction of $\text{NH}_4^+$ produced	$\gamma_{\text{NH}_4, \text{DNRA}2}$	Lognormal	0.226	10%	Stoichiometry	<u>0.22 (± 0.02)</u>	
Anammox	Reaction rate factor	$f_{\text{Anam}, \text{Den}2}$	Lognormal	0.2	25%	$^{15}\text{N}$ -tracer incubations (this study)	<u>0.20 (± 0.03)</u>	
	$\text{O}_2$ inhibition constant	$K_{\text{O}_2, \text{Anam}}$	Lognormal	2.5 $\mu\text{M}$	20%	(Kalvelage et al., 2011)	<u>2.5 (± 0.3) <math>\mu\text{M}</math></u>	
	$\text{NH}_4^+$ limitation constant	$K_{\text{NH}_4, \text{Anam}}$	Lognormal	1 $\mu\text{M}$	20%	(Wenk et al., 2014)	<u>1.0 (± 0.1) <math>\mu\text{M}</math></u>	
	$\text{NO}_3^-$ limitation constant	$K_{\text{NO}_3, \text{Anam}}$	Lognormal	5 $\mu\text{M}$	20%	Reported for $\text{NO}_3^-$ (Wenk et al. 2014)	<u>5.0 (± 0.7) <math>\mu\text{M}</math></u>	
	$\text{NO}_3^-$ production factor	$f_{\text{Anam, side}}$	Lognormal	0.3	10%	(Brunner et al., 2013)	<u>0.30 (± 0.04)</u>	
(B) <u>Isotope effects, boundary conditions and <math>\delta^{15}\text{N}</math></u>								
Nitritification	[1a]	$\text{NH}_4^+ \rightarrow \text{NO}_2^-$	$\mathcal{E}_{\text{NH}_4, \text{NO}2}$	Normal	30‰	5‰	(Dale et al., 2022; Denk et al., 2017)	<u>11.9 (± 2.2) ‰</u>
	[1b]	$\text{NH}_4^+ \rightarrow \text{N}_2\text{O}$	$\mathcal{E}_{\text{NH}_4, \text{N}_2\text{O}}$	Normal	40‰	5‰	(Denk et al., 2017)	<u>36.3 (± 2.2) ‰</u>
Denitrification	[2]	$\text{NO}_2^- \rightarrow \text{NO}_3^-$	$\mathcal{E}_{\text{NO}2}$	Normal	-13‰	5‰	(Denk et al., 2017)	<u>-6.0 (± 3.1) ‰</u>
	[1]	$\text{NO}_3^- \rightarrow \text{NO}_2^-$	$\mathcal{E}_{\text{Den}}$	Normal	20‰	5‰	(Rooze and Meile 2016; A. W. Dale et al. 2019)	<u>2.8 (± 1.1) ‰</u>
DNRA	[2]	$\text{NO}_2^- \rightarrow \text{N}_2\text{O}$	$\mathcal{E}_{\text{Den}2}$	Normal	15‰	5‰	(Dale et al., 2019; Denk et al., 2017)	<u>7.9 (± 2.9) ‰</u>
	[3]	$\text{N}_2\text{O} \rightarrow \text{N}_2$	$\mathcal{E}_{\text{Den}3}$	Normal	9‰	5‰	(Wenk et al., 2016)	<u>8.3 (± 3.3) ‰</u>
	[1]	$\text{NO}_3^- \rightarrow \text{NO}_2^-$	$\mathcal{E}_{\text{DNRA}}$	Normal	20‰	5‰	(Rooze and Meile 2016; A. W. Dale et al. 2019)	<u>20.0 (± 2.9) ‰</u>

<u>Anammox</u>	[2]	$\text{NO}_2^- \rightarrow \text{NH}_4^+$	$\mathcal{E}_{\text{DNR4.2}}$	Normal	15‰	5‰	$15.6 (\pm 3.0) \text{ ‰}$
		$\text{NH}_4^+ \rightarrow \text{N}_2$	$\mathcal{E}_{\text{Anam. NH4}}$	Normal	23‰	5‰	$17.2 (\pm 3.5) \text{ ‰}$
		$\text{NO}_2^- \rightarrow \text{N}_2$	$\mathcal{E}_{\text{Anam. NO2}}$	Normal	16‰	5‰	$14.4 (\pm 3.0) \text{ ‰}$
		$\text{NO}_2^- \rightarrow \text{NO}_3^-$	$\mathcal{E}_{\text{Anam. NO3}}$	Normal	-31‰	5‰	$-30.0 (\pm 2.7) \text{ ‰}$
		<u>Lower boundary conditions</u>	$\mathcal{E}_{\text{Anam. side}}$	<u>Uniform</u>	<u>-</u>	<u>-</u>	<u>- 8.4 (\pm 0.5) <math>\text{mmol cm}^{-2} \text{ d}^{-1}</math></u>
			$E_{\text{NH4}}$	<u>Uniform</u>	<u>-</u>	<u>-</u>	<u><math>2.0 (\pm 0.5) \text{ ‰}</math></u>
			$\delta^{15}\text{N}_{\text{NH4}}$	<u>Uniform</u>	<u>-</u>	<u>-</u>	<u><math>2.1 (\pm 0.4) \text{ ‰}</math></u>
		<u>Organic Matter isotopic composition</u>	$\delta^{15}\text{N-OM}$	Normal	3‰	0.5‰	(Baumann et al., 2024)
<b>(C) One-step denitrification</b>							
<u>Denitrification</u>		Maximum conversion rate	$k_{\text{Den}}$	Uniform	-	-	$765 (\pm 114) \text{ } \mu\text{M d}^{-1}$
		$\text{O}_2$ inhibition constant	$K_{\text{O2,Den}}$	Lognormal	3 $\mu\text{M}$	20%	$2.9 (\pm 0.4) \text{ } \mu\text{M}$
		$\text{NO}_3^-$ limitation constant	$K_{\text{NO3,Den}}$	Lognormal	2.46 $\mu\text{M}$	20%	$2.2 (\pm 0.3) \text{ } \mu\text{M}$
		Fraction of $\text{NH}_4^+$ produced	$\gamma_{\text{NH4,Den}}$	Lognormal	0.189	10%	$0.17 (\pm 0.01)$
		Isotope effect	$\mathcal{E}_{\text{Den}}$	Normal	20‰	5‰	$5.5 (\pm 0.9) \text{ ‰}$
<u>DNRA</u>	[1]	Reaction rate factor	$f_{\text{DNR4.1,Den}}$	Lognormal	0.005	25%	$0.005 (\pm 0.001)$
	[2]	Reaction rate factor	$f_{\text{DNR4.2,Den}}$	Lognormal	0.005	25%	$0.005 (\pm 0.001)$
	Anammox	Reaction rate factor	$f_{\text{Anam,Den}}$	Lognormal	0.6	25%	$0.6 (\pm 0.1)$

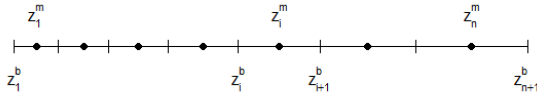
860 **Appendix D: Model discretization**

861 We discretize the partial differential equations outlined in Appendix B using the Method of Lines. This approach involves  
 862 explicit discretization in space, followed by the application of an ODE solver to the resulting system of ODEs.

863 Spatial discretization

864 Numerical discretization of sediment layer ( $n$  cells, cell expansion factor  $f$ ):

865 Visualization:



866

867 Cell boundaries ( $i = 1, \dots, n + 1$ ):

$$868 z_i^b = \begin{cases} \frac{i-1}{n} d & \text{for } f < 1.1 \quad (i = 1, \dots, n+1) \\ \frac{f^{\frac{i-1}{n}} - 1}{f - 1} d & \text{for } f \geq 1.1 \quad (i = 1, \dots, n+1) \end{cases}$$

869 Cell midpoints ( $i = 1, \dots, n$ ):

$$870 z_i^m = \frac{1}{2} (z_i^b + z_{i+1}^b)$$

871 Explanation for the cell expansion factor:

872 The cell size is approximately (the larger  $n$  the closer) proportional to

$$873 \frac{\partial z_i^b}{\partial i} = \frac{\partial}{\partial i} \left( \frac{f^{\frac{i-1}{n}} - 1}{f - 1} d \right) = \frac{\log(f)}{f - 1} \frac{1}{n} f^{\frac{i-1}{n}} d$$

874 Comparing these cell sizes at the lower and upper boundaries leads to

$$875 \frac{\frac{\partial z_i^b}{\partial i} \Big|_{i=n+1}}{\frac{\partial z_i^b}{\partial i} \Big|_{i=1}} = f$$

876 This expression clarifies the meaning of the cell expansion factor (approximately equal to the ratio of cell size of lowest to  
 877 uppermost cell).

878 Discretized Ordinary Differential Equations

879 Mass balance within sediment layer cells ( $i = 2, \dots, n - 1$ ):

$$880 p(z_i^m) \frac{\partial C}{\partial t} (z_i^m) (z_{i+1}^b - z_i^b) \\ 881 = -p(z_i^b) D(z_i^b) \frac{C(z_i^m) - C(z_{i-1}^m)}{z_i^m - z_{i-1}^m} + p(z_{i+1}^b) D(z_{i+1}^b) \frac{C(z_{i+1}^m) - C(z_i^m)}{z_{i+1}^m - z_i^m} \\ 882 + p(z_i^m) r(z_i^m) (z_{i+1}^b - z_i^b)$$

883 Differential equation for concentrations at cell midpoints of inner cells ( $i = 2, \dots, n - 1$ ):

$$884 \frac{\partial C}{\partial t} (z_i^m) = \frac{-p(z_i^b) D(z_i^b) \frac{C(z_i^m) - C(z_{i-1}^m)}{z_i^m - z_{i-1}^m} + p(z_{i+1}^b) D(z_{i+1}^b) \frac{C(z_{i+1}^m) - C(z_i^m)}{z_{i+1}^m - z_i^m}}{p(z_i^m) (z_{i+1}^b - z_i^b)} + r(z_i^m)$$

885 Boundary conditions:

886  $C(z_1^b) = C_0, D(z_{n+1}^b, t)p(z_{n+1}^b, t) \frac{C(z_{n+1}^b) - C(z_n^m)}{z_{n+1}^b - z_n^m} = F_d$

887  $\rightarrow C(z_{n+1}^b) = C(z_n^m) + F_d \frac{z_{n+1}^b - z_n^m}{D(z_{n+1}^b, t)p(z_{n+1}^b, t)}$

888 Differential equations for concentrations at cell midpoints of top and bottom cell ( $i = 1, i = n$ ):

889  $\frac{\partial C}{\partial t}(z_1^m) = \frac{-p(z_1^b)D(z_1^b) \frac{C(z_1^m) - C(z_1^b)}{z_1^m - z_1^b} + p(z_2^b)D(z_2^b) \frac{C(z_2^m) - C(z_1^m)}{z_2^m - z_1^m}}{p(z_1^m)(z_2^b - z_1^b)} + r(z_1^m)$

890  $\frac{\partial C}{\partial t}(z_n^m) = \frac{-p(z_n^b)D(z_n^b) \frac{C(z_n^m) - C(z_{n-1}^m)}{z_n^m - z_{n-1}^m} + p(z_{n+1}^b)D(z_{n+1}^b) \frac{C(z_{n+1}^b) - C(z_n^m)}{z_{n+1}^b - z_n^m}}{p(z_n^m)(z_{n+1}^b - z_n^b)} + r(z_n^m)$

891  $= \frac{-p(z_n^b)D(z_n^b) \frac{C(z_n^m) - C(z_{n-1}^m)}{z_n^m - z_{n-1}^m} + F_d}{p(z_n^m)(z_{n+1}^b - z_n^b)} + r(z_n^m)$

892 **Appendix E: Model implementation**

893 The model was implemented in Julia (Bezanson et al., 2017) (<https://julialang.org>). The implementation is available with  
894 open access at <https://gitlab.com/p.reichert/Nsediment>. The version used for this study corresponds to commit  
895 7afecd1af871e8f8030360d658ec1cf54d20716.

896 The partial differential equations described in Appendix B were spatially discretized according to the approach outlined in  
897 Appendix D. The resulting ordinary differential equations were then numerically solved by the Method of Lines using the  
898 package DifferentialEquations.jl (Rackauckas and Nie, 2017). Discretizing the modelled sediment layer into 50 cells, and  
899 considering 14 state variables, resulted in a system of 700 ordinary differential equations. The performance of several ODE  
900 solvers was compared, resulting in the use of the adaptive order and adaptive time step backward-differencing solver FBDF  
901 to account for the stiffness of the ODE system.

902 Maintaining compatibility with automatic differentiation while allowing flexible parameter selection for inference was a key  
903 implementation challenge. This was addressed by using separate arrays for parameter values and names, and by prepending  
904 the parameters to be estimated, ensuring a contiguous array of the parameters. To avoid inefficiencies related to the search of  
905 parameter names, the association of parameter names to array indices was resolved within the differential equation solver  
906 function. This solver, which includes the function to calculate the right-hand side of the differential equation as an internal  
907 function, ensures that the index resolution has to be done only once and remains available for all calls of the integrator by the  
908 solver. This approach enabled compatibility of our implementation with the automatic differentiation package ForwardDiff.jl  
909 (Revels et al., 2016).

910 Bayesian inference was implemented with both an adaptive Metropolis sampler from the AdaptiveMCMC package (Vihola,  
911 2020) and the Hamiltonian Monte Carlo algorithm from the AdvancedHMC.jl package (Xu et al., 2020).

912 All model outputs were written to text files and post-processed using R (<https://www.r-project.org>).

913 **Code and data availability**

914 The code for the isotope model presented in this manuscript is available at <https://gitlab.com/p.reichert/Nsediment> (commit  
915 7afeedf1af871e8f8030360d658ec1cf54d20716).  
916 Field data, model outputs and re-processing scripts are available through zenodo at  
917 <https://doi.org/10.5281/zenodo.14913873>.

918 **Supplement link**

919 Supplementary material is provided alongside this manuscript.

920 **Author contribution**

921 The research was initiated and conceptually designed by AM, PR, and MFL. All co-authors contributed to the  
922 conceptualization of the model, AM and PR developed the model code and performed the simulations. AM and PR prepared  
923 the manuscript with input from all co-authors.

924 **Competing interests**

925 The authors declare that they have no conflict of interest.

926 **Acknowledgments**

927 Calculations were performed at sciCORE (<http://scicore.unibas.ch/>), the scientific computing centre at the University of  
928 Basel. We thank Prof. Carsten Schubert for providing logistic support for access to Lake Lucerne, and the technical staff at  
929 University of Basel and Eawag for their assistance with the field campaign and the resulting analytical work.  
930 AI-based language tools were used on individual sentences to refine sentence structures and enhance the readability of the  
931 manuscript.

932 **Financial support**

933 This study was funded by the Swiss National Science Foundation, grant SNSF 188728.

934 **References**

935 Andrieu, C., De Freitas, N., Doucet, A., and Jordan, M. I.: An introduction to MCMC for Machine Learning, *Mach. Learn.*,  
936 50, 5–43, <https://doi.org/10.1023/A:1020281327116>, 2003.  
937 Baumann, K. B. L., Mazzoli, A., Salazar, G., Ruscheweyh, H.-J., Müller, B., Niederdorfer, R., Sunagawa, S., Lever, M. A.,  
938 Lehmann, M. F., and Bürgmann, H.: Metagenomic and -transcriptomic analyses of microbial nitrogen transformation  
939 potential, and gene expression in Swiss lake sediments, *ISME Communications*, 4, ycae110,  
940 <https://doi.org/10.1093/ismeco/ycae110>, 2024.  
941 Bender, M., Martin, W., Hess, J., Sayles, R., Ball, L., and Lambert, C.: A whole-core squeezer for interfacial pore-water  
942 sampling, *Limnol. Oceanogr.*, 32, 1214–1225, <https://doi.org/10.4319/lo.1987.32.6.1214>, 1987.

943 Bernardo, J. M. and Smith, A. F. M.: Bayesian Theory, John Wiley & Sons, New York,  
944 <https://doi.org/10.1002/9780470316870>, 1994.

945 Betancourt, M.: A conceptual introduction to Hamiltonian Monte Carlo, arXiv: Statistics, Methodology,  
946 <https://doi.org/10.48550/arXiv.1701.02434>, 2017.

947 Bezanson, J., Edelman, A., Karpinski, S., and Shah, V. B.: Julia: A fresh approach to numerical computing, SIAM Review,  
948 59, 65–98, <https://doi.org/10.1137/14100671>, 2017.

949 Brunner, B., Contreras, S., Lehmann, M. F., Matantseva, O., Rollog, M., Kalvelage, T., Klockgether, G., Lavik, G., Jetten,  
950 M. S. M., Kartal, B., and Kuypers, M. M. M.: Nitrogen isotope effects induced by anammox bacteria, Proc. Natl. Acad. Sci.  
951 U. S. A., 110, 18994–18999, <https://doi.org/10.1073/pnas.1310488110>, 2013.

952 Buchwald, C., Hornola, K., Spivack, A. J., Estes, E. R., Murray, R. W., and Wankel, S. D.: Isotopic constraints on nitrogen  
953 transformation rates in the deep sedimentary marine biosphere, Global Biogeochem. Cycles, 32, 1688–1702,  
954 <https://doi.org/10.1029/2018GB005948>, 2018.

955 Burdige, D. J.: Chapter 6: Models of sediment diagenesis, in: Geochemistry of Marine Sediments, Princeton, 72–96,  
956 <https://doi.org/10.1515/9780691216096-008>, 2007.

957 Casciotti, K. L.: Inverse kinetic isotope fractionation during bacterial nitrite oxidation, Geochim. Cosmochim. Acta, 73,  
958 2061–2076, <https://doi.org/10.1016/j.gca.2008.12.022>, 2009.

959 Casciotti, K. L., Sigman, D. M., Hastings, M. G., Böhlke, J. K., and Hilkert, A.: Measurement of the oxygen isotopic  
960 composition of nitrate in seawater and freshwater using the denitrifier method, Anal. Chem., 74, 4905–4912,  
961 <https://doi.org/10.1021/ac020113w>, 2002.

962 Crowe, S. A., Treusch, A. H., Forth, M., Li, J., Magen, C., Canfield, D. E., Thamdrup, B., and Katsev, S.: Novel anammox  
963 bacteria and nitrogen loss from Lake Superior, Sci. Rep., 7, 13757, <https://doi.org/10.1038/s41598-017-12270-1>, 2017.

964 Dale, A. W., Bourbonnais, A., Altabet, M., Wallmann, K., and Sommer, S.: Isotopic fingerprints of benthic nitrogen cycling  
965 in the Peruvian oxygen minimum zone, Geochim. Cosmochim. Acta, 245, 406–425,  
966 <https://doi.org/10.1016/j.gca.2018.10.025>, 2019.

967 Dale, A. W., Clemens, D., Dähnke, K., Korth, F., Wankel, S. D., Schroller-Lomnitz, U., Wallmann, K., and Sommer, S.:  
968 Nitrogen cycling in sediments on the NW African margin inferred from N and O isotopes in benthic chambers, Front. Mar.  
969 Sci., 9, 902062, <https://doi.org/10.3389/fmars.2022.902062>, 2022.

970 Denk, T. R. A., Mohn, J., Decock, C., Lewicka-Szczebak, D., Harris, E., Butterbach-Bahl, K., Kiese, R., and Wolf, B.: The  
971 nitrogen cycle: A review of isotope effects and isotope modeling approaches, Soil Biol. Biochem., 105, 121–137,  
972 <https://doi.org/10.1016/j.soilbio.2016.11.015>, 2017.

973 Drury, C. F., Tel, D. A., and Beauchamp, E. G.:  $^{15}\text{N}$  analysis of highly enriched samples of a mass spectrometer, Can. J. Soil  
974 Sci., 67, 779–785, <https://doi.org/10.4141/cjss87-075>, 1987.

975 Frey, C., Dippner, J. W., and Voss, M.: Close coupling of N-cycling processes expressed in stable isotope data at the  
976 redoxcline of the Baltic Sea, Global Biogeochem. Cycles, 28, 974–991, <https://doi.org/10.1002/2013GB004642>, 2014.

977 Gelman, A., Carlin, J. B., Stern, H. S., Dunson, D. B., Vehtari, A., and Rubin, D. B.: Bayesian Data Analysis, 2<sup>nd</sup> ed.,  
978 Chapman and Hall/CRC, <https://doi.org/10.1201/b16018>, 2013.

979 Granger, J. and Wankel, S. D.: Isotopic overprinting of nitrification on denitrification as a ubiquitous and unifying feature of  
980 environmental nitrogen cycling, Proc. Natl. Acad. Sci. U. S. A., 113, E6391–E6400,  
981 <https://doi.org/10.1073/pnas.1601383113>, 2016.

982 Guillaume, J. H. A., Jakeman, J. D., Marsili-Libelli, S., Asher, M., Brunner, P., Croke, B., Hill, M. C., Jakeman, A. J.,  
983 Keesman, K. J., Razavi, S., and Stigter, J. D.: Introductory overview of identifiability analysis: A guide to evaluating  
984 whether you have the right type of data for your modeling purpose, Environmental Modelling and Software, 119, 418–432,  
985 <https://doi.org/10.1016/j.envsoft.2019.07.007>, 2019.

986 Hines, D. E., Lisa, J. A., Song, B., Tobias, C. R., and Borrett, S. R.: A network model shows the importance of coupled  
987 processes in the microbial N cycle in the Cape Fear River Estuary, *Estuar. Coast Shelf. Sci.*, 106, 45–57,  
988 <https://doi.org/10.1016/j.ecss.2012.04.018>, 2012.

989 Holtappels, M., Lavik, G., Jensen, M. M., and Kuypers, M. M. M.:  $^{15}\text{N}$ -labeling experiments to dissect the contributions of  
990 heterotrophic denitrification and anammox to nitrogen removal in the OMZ waters of the ocean, in: *Methods in*  
991 *Enzymology*, 486, 223–251, [https://doi.org/10.1016/S0076-6879\(11\)86010-6](https://doi.org/10.1016/S0076-6879(11)86010-6), 2011.

992 Ibáñez, J. S. P. and Rocha, C.: Kinetics of inorganic nitrogen turnover in a sandy seepage face on a subterranean estuary,  
993 *Appl. Geochem.*, 87, 108–121, <https://doi.org/10.1016/j.apgeochem.2017.10.015>, 2017.

994 Jensen, M. M., Lam, P., Revsbech, N. P., Nagel, B., Gaye, B., Jetten, M. S., and Kuypers, M. M.: Intensive nitrogen loss  
995 over the Omani Shelf due to anammox coupled with dissimilatory nitrite reduction to ammonium, *ISME J.*, 5, 1660–1670,  
996 <https://doi.org/10.1038/ismej.2011.44>, 2011.

997 Ji, Q., Buitenhuis, E., Suntharalingam, P., Sarmiento, J. L., and Ward, B. B.: Global nitrous oxide production determined by  
998 oxygen sensitivity of nitrification and denitrification, *Global Biogeochem. Cycles*, 32, 1790–1802,  
999 <https://doi.org/10.1029/2018GB005887>, 2018.

1000 Kalvelage, T., Jensen, M. M., Contreras, S., Revsbech, N. P., Lam, P., Günter, M., LaRoche, J., Lavik, G., and Kuypers, M.  
1001 M. M.: Oxygen sensitivity of anammox and coupled N-cycle processes in oxygen minimum zones, *PLoS One*, 6, e29299,  
1002 <https://doi.org/10.1371/journal.pone.0029299>, 2011.

1003 Kampschreur, M. J., Kleerebezem, R., Picioreanu, C., Bakken, L., Bergaust, L., de Vries, S., Jetten, M. S. M., and van  
1004 Loosdrecht, M. C. M.: Metabolic modeling of denitrification in *Agrobacterium tumefaciens*: A tool to study inhibiting and  
1005 activating compounds for the denitrification pathway, *Front. Microbiol.*, 3, 370, <https://doi.org/10.3389/fmicb.2012.00370>,  
1006 2012.

1007 Kessler, A. J., Bristow, L. A., Cardenas, M. B., Glud, R. N., Thamdrup, B., and Cook, P. L. M.: The isotope effect of  
1008 denitrification in permeable sediments, *Geochim. Cosmochim. Acta*, 133, 156–167,  
1009 <https://doi.org/10.1016/j.gca.2014.02.029>, 2014.

1010 Kraft, B., Strous, M., and Tegetmeyer, H. E.: Microbial nitrate respiration - Genes, enzymes and environmental distribution,  
1011 *J. Biotechnol.*, 155, 104–117, <https://doi.org/10.1016/j.jbiotec.2010.12.025>, 2011.

1012 Lehmann, M. F., Reichert, P., Bernasconi, S. M., Barbieri, A., and McKenzie, J. A.: Modelling nitrogen and oxygen isotope  
1013 fractionation during denitrification in a lacustrine redox-transition zone, *Geochim. Cosmochim. Acta*, 67, 2529–2542,  
1014 [https://doi.org/10.1016/S0016-7037\(03\)00085-1](https://doi.org/10.1016/S0016-7037(03)00085-1), 2003.

1015 Lehmann, M. F., Sigman, D. M., and Berelson, W. M.: Coupling the  $^{15}\text{N}/^{14}\text{N}$  and  $^{18}\text{O}/^{16}\text{O}$  of nitrate as a constraint on benthic  
1016 nitrogen cycling, *Mar. Chem.*, 88, 1–20, <https://doi.org/10.1016/j.marchem.2004.02.001>, 2004.

1017 Lehmann, M. F., Sigman, D. M., McCorkle, D. C., Brunelle, B. G., Hoffmann, S., Kienast, M., Cane, G., and Clement, J.:  
1018 Origin of the deep Bering Sea nitrate deficit: Constraints from the nitrogen and oxygen isotopic composition of water  
1019 column nitrate and benthic nitrate fluxes, *Global Biogeochem. Cycles*, 19, GB4005, <https://doi.org/10.1029/2005GB002508>,  
1020 2005.

1021 Lehmann, M. F., Sigman, D. M., McCorkle, D. C., Granger, J., Hoffmann, S., Cane, G., and Brunelle, B. G.: The  
1022 distribution of nitrate  $^{15}\text{N}/^{14}\text{N}$  in marine sediments and the impact of benthic nitrogen loss on the isotopic composition of  
1023 oceanic nitrate, *Geochim. Cosmochim. Acta*, 71, 5384–5404, <https://doi.org/10.1016/j.gca.2007.07.025>, 2007.

1024 Magyar, P. M., Hausherr, D., Niederdorfer, R., Stöcklin, N., Wei, J., Mohn, J., Bürgmann, H., Joss, A., and Lehmann, M. F.:  
1025 Nitrogen isotope effects can be used to diagnose N transformations in wastewater anammox systems, *Sci. Rep.*, 11, 7850,  
1026 <https://doi.org/10.1038/s41598-021-87184-0>, 2021.

1027 Martin, T. S., Primeau, F., and Casciotti, K. L.: Modeling oceanic nitrate and nitrite concentrations and isotopes using a 3-D  
1028 inverse N cycle model, *Biogeosciences*, 16, 347–367, <https://doi.org/10.5194/bg-16-347-2019>, 2019.

1029 McIlvin, M. R. and Casciotti, K. L.: Fully automated system for stable isotopic analyses of dissolved nitrous oxide at natural  
1030 abundance levels, *Limnol. Oceanogr. Methods*, 8, 54–66, <https://doi.org/10.4319/lom.2010.8.54>, 2010.

1031 Neal, R. M.: MCMC using Hamiltonian dynamics, Chapman and Hall/CRC, <https://doi.org/10.1201/b10905-6>, 2011.

1032 Ni, B. J., Ruscalleda, M., Pellicer-Nàcher, C., and Smets, B. F.: Modeling nitrous oxide production during biological  
1033 nitrogen removal via nitrification and denitrification: Extensions to the general ASM models, *Environ. Sci. Technol.*, 45,  
1034 7768–7776, <https://doi.org/10.1021/es201489n>, 2011.

1035 Paraska, D., Hipsey, M. R., and Salmon, S. U.: Comparison of organic matter oxidation approaches in sediment diagenesis  
1036 models, in: 19<sup>th</sup> International Congress on Modelling and Simulation, 3754–3760, 2011.

1037 Pätsch, J. and Kühn, W.: Nitrogen and carbon cycling in the North Sea and exchange with the North Atlantic-A model study.  
1038 Part I. Nitrogen budget and fluxes, *Cont. Shelf Res.*, 28, 767–787, <https://doi.org/10.1016/j.csr.2007.12.013>, 2008.

1039 Rackauckas, C. and Nie, Q.: DifferentialEquations.jl – A Performant and Feature-Rich Ecosystem for Solving Differential  
1040 Equations in Julia, *J. Open Res. Softw.*, 5, 15, <https://doi.org/10.5334/jors.151>, 2017.

1041 Revels, J., Lubin, M., and Papamarkou, T.: Forward-Mode automatic differentiation in Julia,  
1042 <https://doi.org/10.48550/arXiv.1607.07892>, 2016.

1043 Richards, C. M. and Pallud, C.: Kinetics of sulfate reduction and sulfide precipitation rates in sediments of a bar-built  
1044 estuary (Pescadero, California), *Water Res.*, 94, 86–102, <https://doi.org/10.1016/j.watres.2016.01.044>, 2016.

1045 Risgaard-Petersen, N., Nielsen, L. P., Rysgaard, S., Dalsgaard, T., and Meyer, R. L.: Application of the isotope pairing  
1046 technique in sediments where anammox and denitrification coexist, *Limnol. Oceanogr. Methods*, 1, 63–73,  
1047 <https://doi.org/10.4319/lom.2003.1.63>, 2003.

1048 Robert, C. P.: The Bayesian choice - From decision-theoretic foundations to computational implementation, 2<sup>nd</sup> ed.,  
1049 Springer, New York, 2007.

1050 Rooze, J. and Meile, C.: The effect of redox conditions and bioirrigation on nitrogen isotope fractionation in marine  
1051 sediments, *Geochim. Cosmochim. Acta*, 184, 227–239, <https://doi.org/10.1016/j.gca.2016.04.040>, 2016.

1052 Sigman, D. M. and Fripiat, F.: Nitrogen isotopes in the ocean, in: *Encyclopedia of Ocean Sciences*, 3<sup>rd</sup> ed., 1–5, Elsevier,  
1053 <https://doi.org/10.1016/B978-0-12-409548-9.11605-7>, 2019.

1054 Sigman, D. M., Casciotti, K. L., Andreani, M., Barford, C., Galanter, M., and Böhlke, J. K.: A bacterial method for the  
1055 nitrogen isotopic analysis of nitrate in seawater and freshwater, *Anal. Chem.*, 73, 4145–4153,  
1056 <https://doi.org/10.1021/ac010088e>, 2001.

1057 Steinsberger, T., Schwefel, R., Wüest, A., and Müller, B.: Hypolimnetic oxygen depletion rates in deep lakes: Effects of  
1058 trophic state and organic matter accumulation, *Limnol. Oceanogr.*, 65, 3128–3138, <https://doi.org/10.1002/lno.11578>, 2020.

1059 Strous, M., Gijs Kuenen, J., and Jetten, M. S. M.: Key physiology of anaerobic ammonium oxidation, *Appl. Environ.  
1060 Microbiol.*, 65, 3248–3250, <https://doi.org/10.1128/AEM.65.7.3248-3250.1999>, 1999.

1061 Su, X., Zhu, X., Li, J., Wu, L., Li, X., Zhang, Q., and Peng, Y.: Determination of partial denitrification kinetic model  
1062 parameters based on batch tests and metagenomic sequencing, *Bioresour. Technol.*, 379, 128977,  
1063 <https://doi.org/10.1016/j.biortech.2023.128977>, 2023.

1064 Suenaga, T., Aoyagi, R., Sakamoto, N., Riya, S., Ohashi, H., Hosomi, M., Tokuyama, H., and Terada, A.: Immobilization of  
1065 Azospira sp. strain I13 by gel entrapment for mitigation of N<sub>2</sub>O from biological wastewater treatment plants: Biokinetic  
1066 characterization and modeling, *J. Biosci. Bioeng.*, 126, 213–219, <https://doi.org/10.1016/j.jbiosc.2018.02.014>, 2018.

1067 Sun, X., Buchanan, P., Zhang, I. H., Roman, M. S., Babbin, A. R., and Zakem, E.: Ecological dynamics explain modular  
1068 denitrification in the ocean, *Proc. Natl. Acad. Sci. U. S. A.*, 121, e2417421121, <https://doi.org/10.1073/pnas.2417421121>,  
1069 2024.

1070 Thunell, R. C., Sigman, D. M., Muller-Karger, F., Astor, Y., and Varela, R.: Nitrogen isotope dynamics of the Cariaco  
1071 Basin, Venezuela, *Global Biogeochem. Cycles*, 18, GB3001, <https://doi.org/10.1029/2003GB002185>, 2004.

1072 Vihola, M.: Robust adaptive Metropolis algorithm with coerced acceptance rate, *Stat. Comput.*, 22, 997–1008,  
1073 <https://doi.org/10.1007/s11222-011-9269-5>, 2012.

1074 Vihola, M.: Ergonomic and reliable Bayesian inference with adaptive Markov Chain Monte Carlo, in: Wiley StatsRef:  
1075 Statistics Reference Online, Wiley, 1–12, <https://doi.org/10.1002/9781118445112.stat08286>, 2020.

1076 Wang, S., Pi, Y., Song, Y., Jiang, Y., Zhou, L., Liu, W., and Zhu, G.: Hotspot of dissimilatory nitrate reduction to  
1077 ammonium (DNRA) process in freshwater sediments of riparian zones, *Water Res.*, 173, 115539,  
1078 <https://doi.org/10.1016/j.watres.2020.115539>, 2020.

1079 Wankel, S. D., Buchwald, C., Ziebis, W., Wenk, C. B., and Lehmann, M. F.: Nitrogen cycling in the deep sedimentary  
1080 biosphere: Nitrate isotopes in porewaters underlying the oligotrophic North Atlantic, *Biogeosciences*, 12, 7483–7502,  
1081 <https://doi.org/10.5194/bg-12-7483-2015>, 2015.

1082 Wenk, C. B., Zopfi, J., Blees, J., Veronesi, M., Niemann, H., and Lehmann, M. F.: Community N and O isotope  
1083 fractionation by sulfide-dependent denitrification and anammox in a stratified lacustrine water column, *Geochim.  
1084 Cosmochim. Acta*, 125, 551–563, <https://doi.org/10.1016/j.gca.2013.10.034>, 2014.

1085 Wenk, C. B., Frame, C. H., Koba, K., Casciotti, K. L., Veronesi, M., Niemann, H., Schubert, C. J., Yoshida, N., Toyoda, S.,  
1086 Makabe, A., Zopfi, J., and Lehmann, M. F.: Differential N<sub>2</sub>O dynamics in two oxygen-deficient lake basins revealed by  
1087 stable isotope and isotopomer distributions, *Limnol. Oceanogr.*, 61, 1735–1749, <https://doi.org/10.1002/lno.10329>, 2016.

1088 Wunderlin, P., Mohn, J., Joss, A., Emmenegger, L., and Siegrist, H.: Mechanisms of N<sub>2</sub>O production in biological  
1089 wastewater treatment under nitrifying and denitrifying conditions, *Water Res.*, 46, 1027–1037,  
1090 <https://doi.org/10.1016/j.watres.2011.11.080>, 2012.

1091 Wyffels, S., Van Hulle, S. W. H., Boeckx, P., Voleke, E. I. P., Van Cleemput, O., Vanrolleghem, P. A., and Verstraete, W.:  
1092 Modeling and simulation of oxygen-limited partial nitritation in a membrane-assisted bioreactor (MBR), *Biotechnol.  
1093 Bioeng.*, 86, 531–542, <https://doi.org/10.1002/bit.20008>, 2004.

1094 Xu, H., Song, G., Yang, S., Zhu, R., Zhang, G., and Liu, S.: Benthic nitrogen cycling in the deep ocean of the Kuroshio  
1095 Extension region, *Front. Mar. Sci.*, 9, 997810, <https://doi.org/10.3389/fmars.2022.997810>, 2022.

1096 Xu, K., Ge, H., Tebbutt, W., Tarek, M., Trapp, M., and Ghahramani, Z.: AdvancedHMC.jl: A robust, modular and efficient  
1097 implementation of advanced HMC algorithms, 2<sup>nd</sup> Symposium on Advances in Approximate Bayesian Inference,  
1098 *Proceedings of Machine Learning Research* 118, 1–10, 2020.

1099 Yuan, B., Guo, M., Zhou, X., Li, M., and Xie, S.: Defining the sources and the fate of nitrate by using dual isotopes and a  
1100 Bayesian isotope mixing model: Water–nitrate management in cascade dams of Lancang river, *Sci. Total Environ.*, 886,  
1101 163995, <https://doi.org/10.1016/j.scitotenv.2023.163995>, 2023.

1102 Zhang, L., Altabet, M. A., Wu, T., and Hadas, O.: Sensitive measurement of NH<sub>4</sub><sup>+</sup> <sup>15</sup>N/<sup>14</sup>N ( $\delta^{15}\text{NH}_4^+$ ) at natural abundance  
1103 levels in fresh and saltwaters, *Anal. Chem.*, 79, 5297–5303, <https://doi.org/10.1021/ac070106d>, 2007.